Variable Stoichiometry Effects on Glacial/Interglacial Ocean Model Biogeochemical Cycles and Carbon Storage

Nathaniel J. Fillman[1*], Andreas Schmittner[1†], and Karin F. Kvale[2‡]

[1]College of Earth, Ocean, and Atmospheric Sciences, Oregon State University, Corvallis, OR, USA.

[2]Environmental Processes and Modelling, GNS Science, Lower Hutt, New Zealand.

Corresponding author: Nathaniel Fillman (FillmanN@oregonstate.edu)

* https://orcid.org/0000-0002-5380-7495

† https://orcid.org/0000-0002-8376-0843

‡ https://orcid.org/0000-0001-8043-5431

Key Points:

- Variable C:P allows more physiological and ecological interactivity in plankton thereby increasing the biological carbon pump.
- Variable Si:N affects ocean carbon cycling little but better constrains diatom and Si simulations.
- Changes in glacial-interglacial phytoplankton C:P enhances ocean C sequestration and reduces atmospheric CO_2 by 13 – 14 ppm.

Abstract

Realistic model representation of ocean phytoplankton is important for simulating nutrient cycles and the biological carbon pump, which affects atmospheric carbon dioxide (pCO_2) concentrations and, thus, climate. Until recently, most models assumed constant ratios (or stoichiometry) of phosphorous (P), nitrogen (N), silicon (Si), and carbon (C) in phytoplankton, despite observations indicating systematic variations. Here, we investigate the effects of variable stoichiometry on simulated nutrient distributions, plankton community compositions, and the C cycle in the preindustrial (PI) and glacial oceans. Using a biogeochemical model, a linearly increasing P:N relation to increasing PO_4 is implemented for ordinary phytoplankton (P_O), and a nonlinearly decreasing Si:N relation to increasing Fe is applied to diatoms (P_{Diat}). C:N remains fixed. Variable P:N affects modeled community composition through enhanced PO_4 availability, which increases N-fixers in the oligotrophic ocean, consistent with previous research. This increases the NO_3 fertilization of P_O, the NO_3 inventory, and the total plankton biomass. Surface nutrients are not significantly altered. Conversely, variable Si:N shifts south the Southern Ocean's meridional surface silicate gradient, which aligns better with observations, but depresses P_{Diat} growth globally. In Last Glacial Maximum simulations, P_O respond to more oligotrophic conditions by increasing their C:P. This strengthens the biologically mediated C storage such that dissolved organic (inorganic) C inventories increase by 34-40 (38-50) Pg C and 0.7-1.2 Pg yr^{-1} more particulate C is exported into the interior ocean. Thus, an additional 13-14 ppm of pCO_2 difference from PI levels results, improving model agreement with glacial observations.

1. Introduction

Surface ocean plankton redistribute nitrogen (N), phosphorus (P), and carbon (C) to the deep ocean via incomplete respiration of sinking organic matter. Thereafter, respiration continues but remineralized nutrients assume the long residence times of deep ocean water masses, effectively sequestering them from the climate system. This process, known as the biological pump, increases the influx of atmospheric CO_2 (pCO_2) thereby influencing the global climate (McKinley et al., 2017; Sarmiento & Gruber, 2006; Sigman et al., 2010; Volk & Hoffert, 1985). Some C remains bound in the structures of dissolved organic molecules, termed dissolved organic carbon (DOC), but is not significantly chemically reactive to the air-sea exchange (Lønborg et al., 2020). DOC is then an additional long-lasting, depth-independent sink in the

inorganic ocean C cycle that allows further ocean C uptake (Jiao et al., 2010; Lønborg et al., 2020). For simplicity, we include the DOC cycle in the definition of "biological C pump." The oceanic biological carbon pump's influence on the global climate has long been documented (Bisson et al., 2020; Falkowski, 2012; Field et al., 1998; Houghton, 2007; Nowicki et al., 2022). Briefly, oceanic primary producers are estimated to export ~5–12 Pg C yr^{-1} and account for ~50% of the global annual net primary production (NPP), in carbon, matching the terrestrial C-fixation rates (Field et al., 1998; Nowicki et al., 2022). Thus, the biological carbon pump can notably influence climate and must be simulated properly in global climate models.

In 1934, a close correlation between inorganic nutrient and carbon concentrations in the ocean was observed by A. Redfield, leading him to suggest that, on average, plankton have approximately constant C:N:P (Redfield, 1934) and that this ratio controls the relative quantities of biogeochemical elements in ambient seawater (Redfield, 1958). This work has since strongly influenced oceanography including the construction of global models with constant elemental compositions (stoichiometry), which have been the norm until relatively recently (Martiny et al., 2013). Overturning this paradigm is the well-documented adaptability of phytoplankton to nutrient availability variations and recently discovered systematic variations from Redfield's stoichiometry (C. Garcia et al., 2018; N. Garcia et al., 2018; Geider & LaRoche, 2002; Klausmeier et al., 2004; Martiny et al., 2013; Weber & Deutsch, 2010). Phytoplankton, thus, can lower their cellular quota for scarce nutrients while continuing to fix carbon, which is typically more abundant (Galbraith & Martiny, 2015; Klausmeier et al., 2004; Martiny et al., 2013; Moreno & Martiny, 2018).

While computationally inexpensive, the fixed stoichiometry simplification limits realism (Flynn, 2010). The canonical fixed C:N:P of phytoplankton, in addition to fixed Si:N, may be representative of the whole ocean average but its usage in global climate models smooths the spatial variability of the carbon pump. As shown in this study and others, fixed ratios can impede accurate simulations of primary producers, their population dynamics, ocean nutrient distributions, and the biological pump (Galbraith & Skinner, 2020; Matsumoto et al., 2020; Ödalen et al., 2020; Tanioka & Matsumoto, 2017). Model performance is thereby limited in simulating realistic ocean carbon cycling under various climate states. The ocean modeling community has started to include variable stoichiometric ratios in their simulations but few

capture any variability between the three primary macronutrients (C, N, and P) (Séférian et al., 2020). Most of the CMIP 5 and 6 models have fixed ratios or only carry some form of micronutrient to macronutrient variability, e.g., Fe:P (Pahlow et al., 2020; Séférian et al., 2020). Otherwise, only a handful of fully coupled earth systems models use variable macronutrient ratios, of which, three have studied the glacial C cycle implications: MESMO2 (Matsumoto et al., 2020), cGENIE (Ödalen et al., 2020), and CSIRO Mk3L-COAL (Buchanan et al., 2019b). Although, several simple box models have demonstrated the implications of variable stoichiometry (Galbraith & Martiny, 2015; Moreno et al., 2018; Weber & Deutsch, 2010).

Here, we implement variable stoichiometry schemes in an intermediate complexity climate/ocean model to allow a more interactive and responsive ocean carbon cycle. The C:P and Si:N schemes are incrementally applied to individual plankton functional types (PFT) to precisely highlight the full implications of capturing realistic biogeochemical interactions. We also tune the new model slightly in a third experiment. These three configurations will be collectively referred to as the variable stoichiometry models (VSMs).

The ordinary phytoplankton (P_O) C:P increases as ambient PO_4 concentrations decrease, as observed in collected particulate organic matter (POM) (Galbraith & Martiny, 2015; Martiny et al., 2013). The C:P variability can be induced by changes in the relative amounts of organic molecules, e.g., proteins versus RNA, changes in nutrient resource storage, or taxonomic shifts within a community (Geider & La Roche, 2002; Inomura et al., 2022; Liefer et al., 2019). C:N was observed as mostly constant with planktonic heterotrophs exhibiting stable C:N:P (Ho et al., 2020).

Diatoms (P_{Diat}) are phytoplankton that construct siliceous cell walls (or frustules) and contribute to biological C storage not only through comprising a substantial portion (~1/5) of global primary production but also through their frustules-enabled efficient sinking of organic C to the deep ocean (Hildebrand & Lerch, 2015; Lafond et al., 2020; Zúñiga et al., 2021). P_{Diat} continue to consume silicic acid, referred to simply as Si hereafter, from ambient seawater even as other nutrients become scarce. Both in situ observations and culture experiments have shown that the Si:N of P_{Diat} increases as Fe concentration decreases (Franck et al., 2000; Hutchins & Bruland, 1998; Takeda, 1998). It is hypothesized that the formation rate of soft organic P_{Diat}

tissue slows faster with Fe limitations than the formation of hard siliceous tissue (Franck et al., 2000; Meyerink et al., 2017).

The biological carbon pump may thus respond to different environmental and climatic settings through changes in the stoichiometry of phytoplankton (Moreno et al., 2018). The implications of these C:P and Si:N observations on our mechanistic understanding of biosphere-climate interactions are not well understood (Galbraith & Martiny, 2015; Lafond et al., 2020; Moreno et al., 2018; Moreno & Martiny, 2018; Séférian et al., 2020). We attempt, here, to illuminate some of those mechanisms and better understand the Last Glacial Maximum (LGM) to Preindustrial (PI) climate shift which promotes understanding of future climate evolution (Tierney et al., 2020).

Variable stoichiometry may have played a significant role in carbon cycling during past climate states such as the LGM when pCO_2 was 90-100 ppm lower than PI levels (Barnola et al., 1987; Bouttes et al., 2011; Du et al., 2020; Galbraith & Martiny, 2015; Lüthi et al., 2008; Marcott et al., 2014; Petit et al., 1999). The biological carbon pump has been suggested to be partially responsible for this pCO_2 drawdown, but most previous modeling studies used fixed stoichiometric ratios and can only explain a portion of this reduction (Brovkin et al., 2007; Buchanan et al., 2019b; Khatiwala et al., 2019; Kohfeld et al., 2005). Two prior studies that have used flexible stoichiometry (C:P and C:N) noted an additional 11-20 ppm reduction driven by an enhanced ocean biological C storage (Matsumoto et al., 2020; Ödalen et al., 2020).

Here we confirm those results, but we identify additional mechanisms that increase C storage. Larger primary producer biomasses are supported through improved cohabitation between PFTs. We also identify and quantify the DOC component of biological C storage, which responds similarly to variable stoichiometry as the dissolved inorganic C (DIC) inventory. The resulting LGM climate simulations are closer to reconstruction estimates from observed pCO_2 data than simulations without flexible stoichiometry (Bereiter et al., 2015; Ivanovic et al., 2016; Kageyama et al., 2017). Our results suggest that the LGM biological carbon storage was stronger than previous fixed-stoichiometry simulations suggested and likely contributed to the ocean's LGM pCO_2 sequestration (Galbraith & Martiny, 2015; Galbraith & Skinner, 2020; Sigman & Boyle, 2000).

2. Materials and Methods

2.1. Model Description

This study uses the University of Victoria Earth System Climate Model (UVic-ESCM) version 2.9, a three-dimensional ocean general circulation model (GCM) coupled to single-layer atmospheric energy-moisture balance, land surface with dynamic vegetation, and dynamic-thermodynamic sea ice modules (Meissner et al., 2003; Mengis et al., 2020; Weaver et al., 2001). The ocean has a coarse resolution of 3.6° × 1.8° horizontally with 19 vertical levels. Coupled to UVic-ESCM is the Model of Ocean Biogeochemistry and Isotopes (MOBI) version 2.1_08 which simulates interactive nutrient cycles (phosphate (PO_4), nitrate (NO_3), iron (Fe), and silicon (Si)), their associated particulate and dissolved organic phases, oxygen, carbon, detritus, and four PFTs: P_O, diazotrophs (P_{Diaz}) as our N-fixers, P_{Diat}, and zooplankton (P_Z) (Figure 1) (Muglia et al., 2017; Somes et al., 2010; Somes & Oschlies, 2015). Plankton growth rates are Monod functions of nutrients, temperature, and light (Sarmiento & Gruber, 2006). They are structured to consume dissolved organic P (DOP) when it is more plentiful than PO_4; this is not so for DON and NO_3 (Somes & Oschlies, 2015). C:N is 7:1 for all biological variables. In the fixed stoichiometry (*Control*) model, N:P is 16:1 for all plankton except for P_{Diaz} for which it is 40:1. For P_{Diat}, a C:Si of 7.7:1 is used.

While whole ocean P and Si are conserved, the N inventory responds interactively to imbalances between N fixation and denitrification (Kvale et al., 2021). Water column and benthic denitrification schemes, which respire organic matter in suboxic environments ($O_2 < 5$ μM), are described by Somes & Oschlies (2015). N isotopes are traced through the model and are sensitive to biological processes (Schmittner et al., 2013; Somes et al., 2010). Because portions of the ocean C cycling depend on the N cycling, C and Alkalinity are not strictly conserved. Calcium carbonate ($CaCO_3$) and silicon cycling are based on modified models of (Kvale et al., 2015) and (Kvale et al., 2021), respectively. Where applicable, modeled nutrient fields were initialized from World Ocean Atlas, 2013 datasets (H. Garcia et al., 2013; Letscher et al., 2013; Mather et al., 2008).

Upon mortality, plankton's particulate organic matter (POM) is divided into labile, semi-labile, and semi-recalcitrant categories for the mass exchange between various inventories. The

labile POM fraction quickly recycles into inorganic nutrients, the semi-labile into dissolved organic matter (DOM), and the semi-recalcitrant fraction is retained as detrital POM. Particulate organic C (POC) and DOC are implicitly calculated and traced, using C:N, from PON and DON which can remineralize into the explicitly traced DIC. Thus, POC is a source to DOC and DIC, and DOC is a source to DIC. Surface ocean DIC is also regulated by the air-sea gas exchange and is reduced during autotrophy and calcite production. The simulated DOC represents the semi-labile fraction of the observed DOC inventory. We do not simulate the fully recalcitrant DOC fraction described in Lønborg et al. (2020; Somes & Oschlies, 2015).

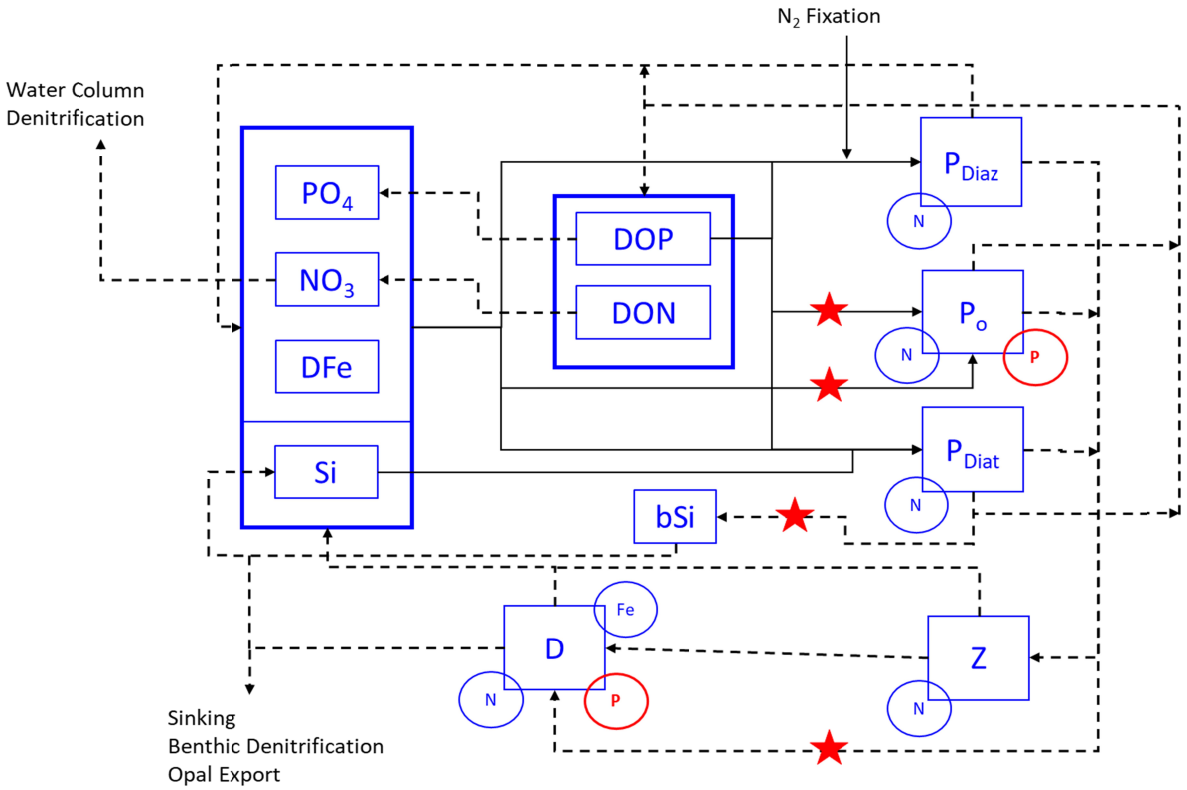

Figure 1. Schematic of MOBI's PFTs and biogeochemical cycles relevant to this study. The red stars indicate where variable stoichiometric schemes were applied. VarP:N is applied at nutrient uptake, while VarSi:N is applied during the implicit computation of biogenic silica. The star on the pathway to the detritus (D) indicates that the VarP:N scheme is communicated to this inventory. The red circled "P" indicates the new prognostic tracers added to MOBI to enable computation of phosphorus content. Solid black lines indicate the flow of nutrients to each

plankton group, while the dashed lines show the flow back into the organic and inorganic inventories.

2.1.1. Variable P:N

Because N is the basic currency for the biological variables in this model, we converted the variable P:C model of Galbraith and Martiny (2015) (hereafter GM15) to a variable P:N model using the constant C:N (Figure 2 and equation 1). For analysis purposes, we use the more intuitive reciprocal (N:P) and the C:P multiple. Tanioka and Matsumoto's (2017) C:P model is neglected here due to its bias toward observed high C:P values at low PO_4. Our P_O, to which variable N:P is applied, inhabit and are the predominant PFT in the low PO_4 domain.

$$P{:}N\ (‰) = 42‰ + 48.3‰\ m^3 mmol^{-1} \times [PO_4(mmol\ m^{-3})] \quad (1)$$

The observations analyzed by GM15 indicate stable C:N ratios over a broad range of surface nutrient concentrations, except for the most oligotrophic waters where little primary production occurs. A variable C:N scheme would thus have little effect on our simulations. Intracellular resource allocation models coupled to GCMs show conflicting results on the stability of C:N, however, their C:P still varies substantially (Inomura et al., 2022; Pahlow et al., 2020). For this reason, and to keep the model computationally efficient, we assume constant C:N throughout every simulation.

Our variable N:P model is only applied to MOBI's P_O. While we recognize the diversity in particle types (e.g., living and nonliving) in the data collected by Martiny et al. (2013) and used to develop the GM15 P:C equation, we also recognize it as a broad, first-order estimation. We then apply it only to the P_O, which is intended to be a representation of unspecialized surface autotrophic plankton, for the following reasons. The P:C observations are biased towards oligotrophic (low PO_4) waters except for the Bering Sea (Martiny et al., 2013). Consequently, the observations preferentially occurred in low silicate environments, implying that siliceous phytoplankton may not be a significant constituent in the collected material (Gregg & Casey, 2007). Thus, the variable N:P model is not extended to our P_{Diat}. Eutrophic (high PO_4) P:C observations are generally at higher latitudes and may then carry a seasonal bias. MOBI also uses the N:P of the well-studied *Trichodesmium* for the simulated P_{Diaz} N:P (P:C of 3.57‰) (Sañudo-Wilhelmy et al., 2004; White et al., 2006). This species inhabits oligotrophic waters and thus

could constitute some of GM15's P:C data. However, there is substantial variability in the observed P:C values at low PO_4 concentrations, and only a minority of these data points are similar to the P_{Diaz} 3.57‰ value. Further, the binned log-transformed means of the data are also substantially higher than this value. Thus, it is unlikely that P_{Diaz} make up any significant portion of the data analyzed by Martiny et al. (2013).

Oceanic heterotroph stoichiometry has been found to be generally more constant and so we do not apply any variability to our P_Z simulations (Galbraith & Martiny, 2015; Ho et al., 2020). Because the P_Z N:P remains fixed, grazing on P_O or detritus is turned off when they have a higher N:P (i.e., a low P content) at low PO_4 concentrations (equation S14). Conversely, in eutrophic waters when P_O or detritus N:P is lower, P_Z only uptake enough P biomass to remain at the constant ratio (N:P = 16:1) with the uptake of the N biomass. The excess P biomass, from this process, is directly routed to the detritus P inventory through "sloppy feeding", a similar convention as used for P_{Diaz} (Somes & Oschlies, 2015).

Two new prognostic equations were implemented in MOBI to explicitly calculate the phosphorus content of both the P_O and the resulting detritus (Figure 1, equations S10 and S12). The latter allows the scheme to affect the biological carbon pump. The variable N:P alters nutrient uptake ratios by proportionally utilizing PO_4 or DOP with respect to the NO_3 according to equation 1 (equations S7 and S8). Two new diagnostic equations were then added to calculate the N:P of P_O ($N:P_{PO}$) and detritus ($N:P_{Detr}$) at every timestep (equation S13), which are subsequently used to calculate the P loss from them (e.g., predation, mortality, remineralization, etc.) (J. Moore et al., 2004).

2.1.2. Variable Si:N

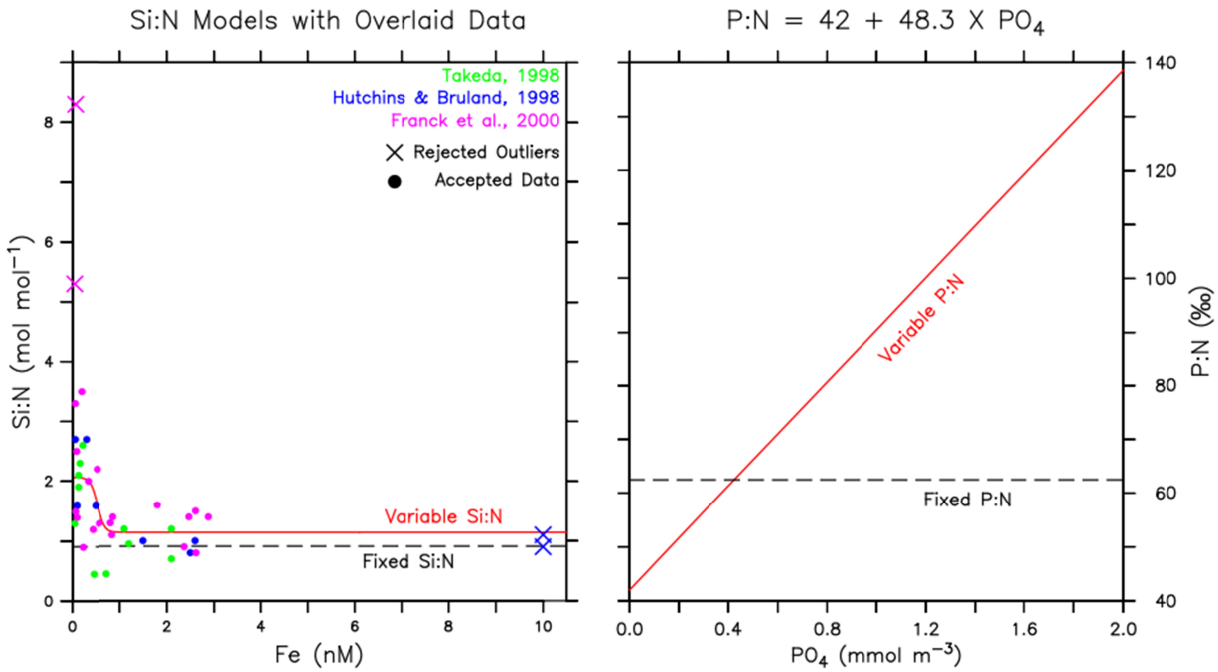

Figure 2. The variable Si:N and P:N models. Left, the variable Si:N was developed from the overlaid data points collected from Franck et al., (2000); Hutchins & Bruland,(1998); and Takeda, (1998). The dashed line is the fixed Si:N from Aumont et al. (2003). The rejected pink outliers were removed as they would increase the maximum Si:N asymptote at low Fe above the majority of the other data points, leading to increased Si consumption and further reducing the accuracy of simulated Si concentrations. The blue outliers were discarded because they do not significantly impact the minimum Si:N asymptote and were only achieved with artificial Fe additions during P_{Diat} culture experiments. Further, Fe at these concentrations is rare in our simulations and is not present in the observed data used to initialize and validate the model. Right, the variable P:N model adapted from Galbraith and Martiny (2015) in red, overlaid with the fixed ratio in the Control simulation.

P_{Diat} Si:N data, in relation to Fe availability, was compiled from three studies to develop a predictive variable Si:N model (Franck et al., 2000; Hutchins & Bruland, 1998; Takeda, 1998). A hyperbolic tangent was fit to the data where the mean Si:N was determined at low Fe concentrations (<0.5 nM) and at high Fe concentrations (≥ 0.5 nM) to define the upper and

lower asymptotes, respectively. Other parameters were determined to achieve the most statistically accurate model possible. The resulting variable Si:N model (Figure 2) is:

$$Si{:}N\ \left(\frac{mol}{mol}\right) = -0.46 \times tanh\left(6.9\, nM^{-1} \times [Fe\ (nM)] - 3.7\right) + 1.6 \quad (2)$$

Equation 2 exhibits similar Si:N values at high Fe as other variable models, except for Holzer et al.'s HYPR experiment (2019; Matsumoto et al., 2013; Matsumoto et al., 2020). While we did not test these exponential models, our Si:N model does allow silica leakage, complimenting their EXP1 and EXP2 findings. Conversely, because we address the large data scatter at low Fe through averaging and outlier rejection, our Si:N model predicts a significantly lower maximum Si:N value than those studies. The variable Si:N scheme serves to regulate the P_{Diat} consumption of Si in addition to the model's preexisting nutrient limitation framework. Biogenic Si is implicitly calculated from the N biomass of P_{Diat} and is only used subsequently in the calculations of opal production and dissolution.

2.2. General Experiment Design

The effects of the VSMs on ocean biogeochemistry were isolated through four different model versions. In *Control*, all stoichiometric ratios are held constant for all PFTs. Note, the N:P of P_{Diaz} differs from that of other plankton but remains constant. Model *VarP:N* applies equation 1 to the P_O and allows this variability to affect the N:P of detritus. The detritus N:P is different from that of the P_O because detritus receives input from all PFTs. Model *VarSi:N* retains *VarP:N* and applies equation 2 to the P_{Diat}. The fourth model, *Tuned*, is identical to *VarSi:N*, except that DOP and DON, referred to collectively as DOM, remineralization rates were accelerated five-fold. This model is an initial attempt at tuning and results in more realistic DOM distributions. Extensive model tuning has not been attempted here and is beyond the scope of this study.

PI and LGM simulations are performed with each model version. The PI simulations were ran for 4,000 model years to reach a climatic and biogeochemical steady state solution. Throughout this spin-up, *p*CO2 was fixed at a preindustrial value of 277 ppm (Bauska et al., 2015). Subsequently, each simulation was ran for an additional 1,000 years with prognostic variable pCO_2 enabled, though these remained close to PI values. LGM boundary conditions were then identically applied and each model ran for an additional 5,000 years with prognostic

275 pCO_2 (Matsumoto et al., 2020), thus allowing the quantification of variable stoichiometry effects
276 on pCO_2 and climate. Analyses were performed on the PI and LGM variable pCO_2 simulations.

277 **2.2.1. Last Glacial Maximum Simulation**

278 LGM boundary conditions are the same as those set forth, and described in detail, by
279 Muglia et al. (2018) except for enabling prognostic pCO_2, which can moderate the simulated
280 climate, and neglecting the reduced sedimentary Fe flux along continental boundaries that was
281 driven by the lower LGM sea levels (Muglia et al., 2017). Tangential simulations exploring the
282 effect of these reduced sedimentary Fe fluxes, in relation to variable stoichiometry, are discussed
283 in section S4. Briefly, the LGM boundary conditions applied identically to all model
284 configurations are: elevated Fe fertilization from increased dust fluxes (south of 35°S these are
285 increased ten-fold), one salinity unit is added to every ocean grid box to account for lower LGM
286 sea levels but the ocean volume remains unchanged, wind stress fields from the PMIP multi-
287 model mean anomaly, decreased southern hemisphere moisture diffusion to increase Antarctic
288 Bottom Water production and meridional extent (Muglia et al., 2018; Muglia & Schmittner,
289 2015), orbital parameters for 21kya (Kageyama et al., 2017), prescribed ICE-6G ice sheets
290 (Peltier et al., 2015), and reduced radiative forcing at the top-of-atmosphere energy budget due to
291 lower atmospheric methane concentrations (Ramaswamy et al., 2001).

292 **2.3. Caveats**

293 There are several important caveats with the model results and the subsequent
294 experiments presented here. Firstly, the terrestrial carbon cycle does not include interactive
295 permafrost, peat, and lithologic weathering. Additionally, a portion (402 Pg) of the land C
296 inventory is instantaneously removed from the earth system with the implementation of the LGM
297 ice sheet mask (Cox, 2001; Meissner et al., 2003). This C is assumed to be buried under the ice
298 and the magnitude is consistent with prior research (Jeltsch-Thommes et al., 2019; Zeng, 2003).
299 The Atlantic Meridional Overturning Circulation (AMOC) strength in the LGM remains
300 uncertain (Muglia et al., 2018). While model results closely match some proxy reconstructions,
301 we cannot assume that the AMOC configuration is correct. We also note that the variable
302 stoichiometry effects on accurately simulating different climate states does depend, sometimes
303 strongly, on how other biologically relevant processes are simulated (section S4).

Several additional simplifications exist in MOBI that may affect our results. P_{Diaz} do not contribute their higher C:N:P to the exported POM and are instead remineralized (J. Moore et al., 2004; Somes & Oschlies, 2015). While our P_{Diaz} have a significantly different C:N:P of 280:40:1, their biomass, relative to other PFTs, is not large. Allowing the excess P_{Diaz} N (and thereby C) to be captured in the detritus inventory increased the global weighted average N:P by 1.2:1 and the export ~ 0.5 Pg C $year^{-1}$ more. The rerouting of this N to the detritus degraded the accuracy of simulated surface PO_4 and NO_3 when compared to observations and so was neglected. Additionally, the ocean model lacks interactive ocean sediments; organic matter is instantly remineralized at the benthic interface and returned to the water column.

There is a significant amount of uncertainty in our DOC quantifications due to the extreme complexity and variability that exists in its sources and heterotrophic processing (Lønborg et al., 2020; Wagner et al., 2020). In MOBI, DOM is simply a parameterized fraction of POM and its recycling varies by temperature. This may explain why the PI DOC is too low compared to prior estimates in *Control, VarP:N, and VarSi:N* (Williams & Druffel, 1987). Alternatively, Somes and Oschlies (2015) suggest the underestimation may be driven by DOM stoichiometry variations. Thus, to achieve the observed quantities, a C:N of 11 is needed to accurately convert DON to DOC. While *Tuned* better matches DON and DOP observations, its DOC is significantly lower than the other simulations and would then require a C:N of 74. Revising the model's DOM cycling is beyond this study's scope; we continue to use a C:N of 7 for DOC computations.

3. Model Validation

3.1 Surface Nutrients

On a global average, *VarP:N* leads to a deterioration of simulated PO_4 and NO_3 distributions, however, most of the error is confined to the Arctic and Southern Oceans (SO). Tuning reverts most of those changes and demonstrates that a model with variable stoichiometry can perform as well as a model with fixed stoichiometry. Introducing *VarSi:N*, conversely, improves simulated Si distributions substantially. Thus, the *Tuned* simulation performs the best, comprehensively. The Taylor diagram (Figure 3) provides a statistical synopsis by plotting the normalized standard deviation (σ) (normalized by the σ of the observations) of a given nutrient

on the radial axis against a simulation's correlation (R) and the uncertainty-corrected root mean square error (RMSE) on the azimuthal axis (Muglia et al., 2018; Taylor, 2001). A perfect simulation would then have a σ and R equal to one, a RMSE of zero, and be collocated with the black dots on the plot. Table S1 details the statistical metrics of the simulated nutrient distributions relative to observed data from the World Ocean Atlas, 2013 (H. Garcia et al., 2013).

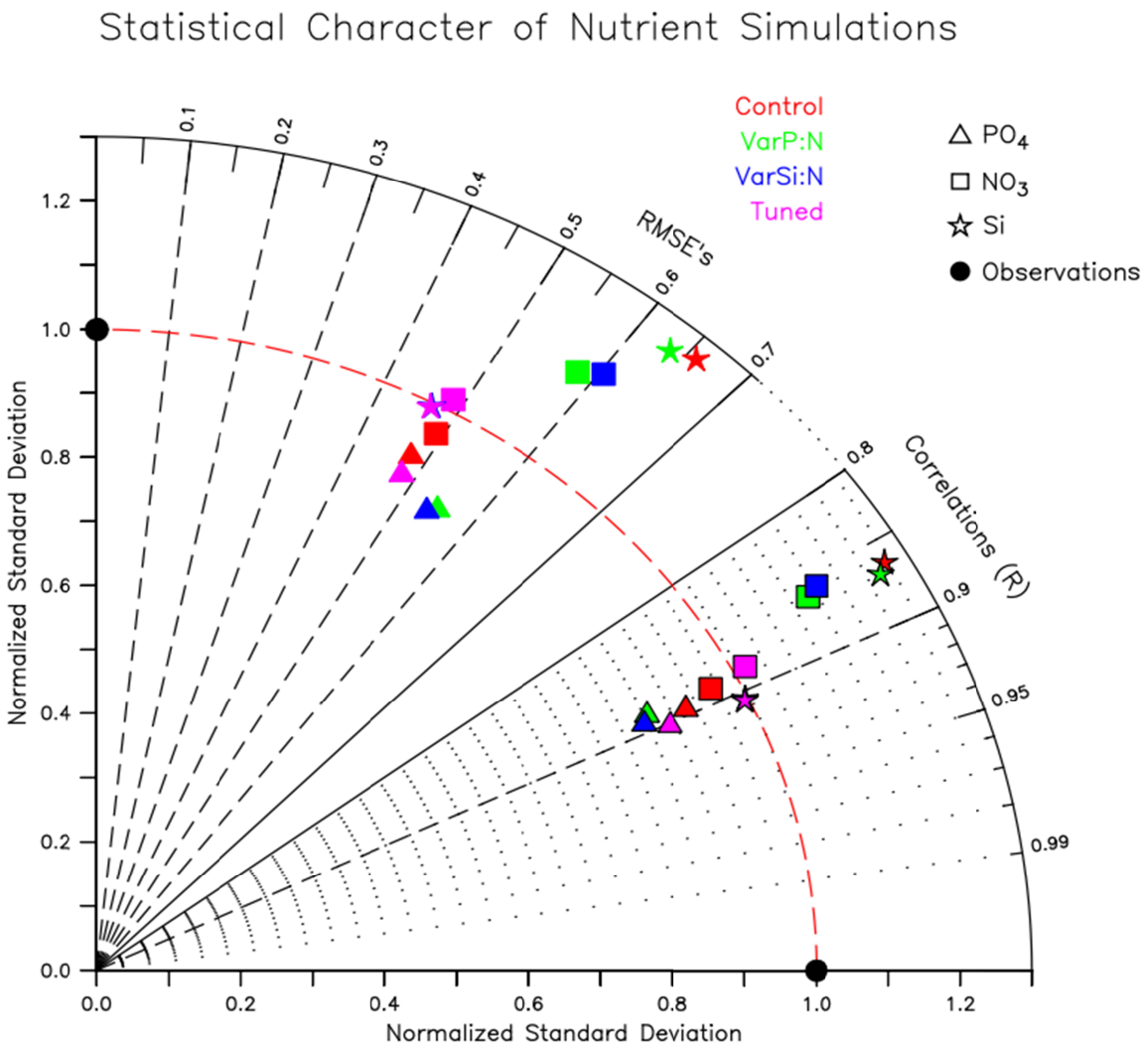

Figure 3. Taylor plot of surface simulated nutrient statistical performance. Perfect performance is indicated by both black circles, thus the proximity to the respective circle can be used to assess a model data point's performance. The dashed red arc indicates a model's nutrient standard deviation matching that of the observed. Symbols with a black outline are plotted against the correlation azimuthal axis, while those without outlines are plotted against the RMSE axis. The

statistical performance of surface Si simulations in VarSi:N and the Tuned models are extremely similar and visual distinction here is difficult.

Contrary to the global perspective, the VSMs had both improving and degrading effects on simulating nutrient spatial distributions, Figure 4 (H. Garcia et al., 2013; Letscher et al., 2013; Mather et al., 2008). Surface NO_3 concentrations improved from the *Control* simulation due to *VarP:N* almost everywhere except at high latitudes. Primary production increases cause more particulate organic N (PON) export to the deep ocean, resulting in waters upwelling with higher NO_3 (Figure S7). Thus, Southern Ocean NO_3, between 30°S and 60°S, now better matches the observations but is still too high closer to the Antarctic margin. Increased simulated NO_3 in the Pacific equatorial and Benguela upwelling currents also improve representations (Figure S1). However, these areas, in addition to the Northwest Pacific, Bering Sea, and the northern Indian Ocean, are still underestimated by *VarP:N* as compared to observations. In the Northeast Atlantic and the Arctic, NO_3 is overestimated by the model. Model resolution and isolation of the Arctic Ocean from the Pacific leads to unrealistically high nutrient concentrations there. However, model-observation differences in ice-covered polar oceans may also be due to seasonal biases in the observations, which lack winter data. The North Atlantic NO_3 overestimation, an increase from the *Control* experiment, is caused by *VarP:N* reducing the PO_4 limitation there and allowing more N-fixation, discussed later.

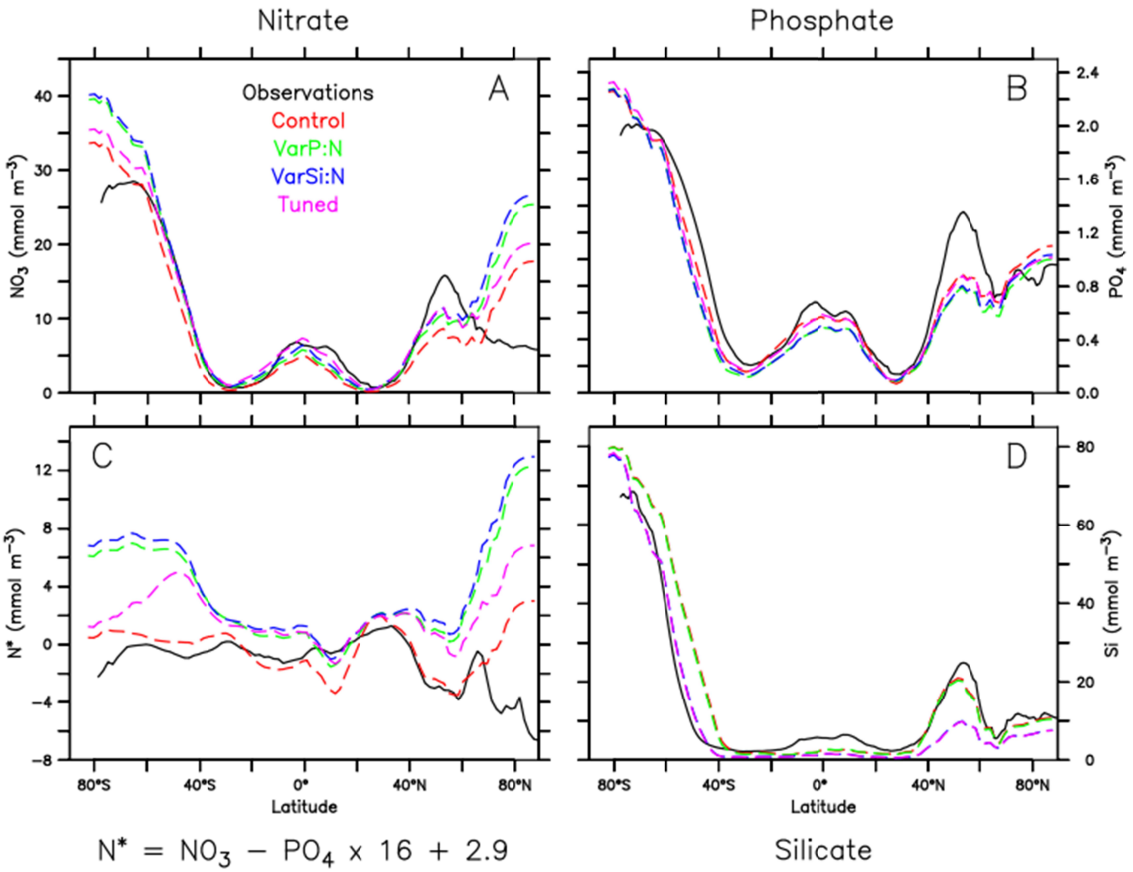

Figure 4. Zonally averaged surface nutrient concentration comparison. Observation are from the World Ocean Atlas, 2013 (H. Garcia et al., 2013). N^* expresses the deviation of the ambient NO_3:PO_4 from the fixed plankton N:P based on the assumption that these ratios are coupled (Redfield, 1934, 1958).

The *Tuned* model increased the extent of the elevated NO_3 concentrations, compared to the *Control*, in the tropical Pacific equatorial upwelling region. However, this area still underestimates in the East Pacific. The tuning decreased NO_3 in the Southern and Arctic Oceans, which improves the agreement with observations there, but had little effect on the NO_3 concentrations in the Bering Sea. Briefly, *VarP:N* degraded $\delta^{15}N$ simulations in the PI and LGM due to the increased export of organic matter, which upon microbial respiration depleted O_2 concentrations, thus increasing denitrification in the interior ocean and inciting more N isotope fractionation (section S5 and Figure S7). The *Tuned* model reduced the $\delta^{15}N$ inaccuracies, compared to the *Control*, in the surface ocean and only slightly degraded representations in the interior.

In contrast to NO_3, PO_4 concentrations were slightly reduced across all latitudes (Figure 4B) in response to *VarP:N*, amplifying the biases from the *Control* (Figure S2). Although P_O are now more P frugal in oligotrophic environments, their increased P use in eutrophic regions and the improved cohabitation with P_{Diaz} overcame this effect, leading to reduced ambient concentrations. Model tuning returns simulation accuracy to approximately that of the *Control*. Regardless, when considering the global C-fixation perspective, the simulated PO_4 underestimation is a lesser concern since PO_4 is only a limiting nutrient after Fe and NO_3 (discussed later), indicating that our primary producers and associated carbon pump are predominantly controlled by other nutrient availabilities.

3.2 Deviations from Fixed Stoichiometry (N*)

Deviations from constant stoichiometry may be captured through $N^* = NO_3 - 16 \times PO_4 + 2.9$ (mmol m^{-3}), but N* is controlled by many processes in addition to stoichiometry (Gruber & Sarmiento, 1997; Monteiro & Follows, 2012; Sarmiento & Gruber, 2006; Weber & Deutsch, 2010). Figure 4C shows N* only in the surface ocean to avoid denitrification influences but upwelling sites may still imprint interior denitrification errors on N*. Surface N* is susceptible to N-fixation which is confined between 40°S and 40°N. All model versions have preferential DOP remineralization but it lacks the spatial variability seen in observations (Clark et al., 1998; Monteiro & Follows, 2012). The cause, whether it be PO_4 or NO_3 inaccuracies (section S1.3), of model departures from observed N* alternate by latitude and regionally. In all model versions, there is a relative excess of NO_3 at the high latitudes (>60°), in the northwest North Pacific and the North Atlantic, along with relatively too little PO_4 in the midlatitudes and tropics (Figures S5 – S6).

The *Control* simulation reproduces the meridional distribution of N* most accurately overall. N* errors in the VSMs mostly stem from inaccuracies in N cycling outside of the euphotic zone, as indicated by relatively high NO_3 at upwelling sites (Figure S5). The excess N stimulates P_{Diat} growth, increasing the P consumption across the SO nutrient gradient (~ 65 – 35°S), and yields excess N* there (Figure 4C and S11). Under *VarP:N*, P_O are only a majority of the population at PO_4 concentrations lower than ~0.1 mmol m^{-3} and are less than 20% of the population at concentrations greater than ~0.55 mmol m^{-3} (Figure 5). Thus, the areas where P_O are most prevalent, generally between 10 and 40°N and °S (Figure 4C and Figure S13),

correspond to the most accurate PO_4 and N* simulations while under *VarP:N* and are not likely the direct cause of the high-latitude N* errors. The other experiments show similar patterns. Alternatively, deep ocean circulations may be inaccurate and cause too much nutrient storage at depth. As suggested by Weber and Deutsch (2010), flexible P_{Diat} N:P may alleviate the SO nutrient gradient error by increasing P consumption at high PO_4 and decreasing it at low PO_4. This, along with further tuning of the N cycle, is likely needed to reduce VSM N* biases. Briefly, the North Atlantic (>40°N) is another notable area of elevated N* values that are driven by higher mid-latitude N-fixation in *VarP:N* which, subsequently, causes more NO_3 to be advected northward.

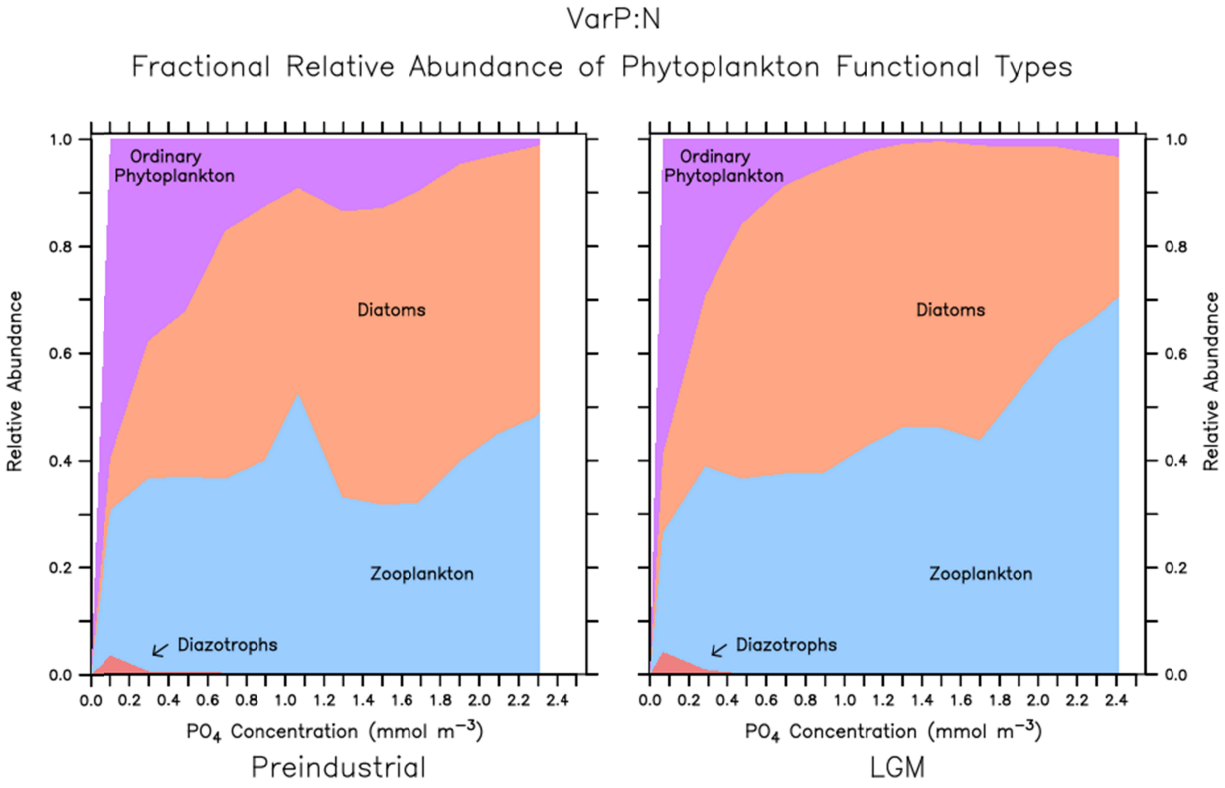

Figure 5. The fractional relative abundance of each PFT against PO_4 concentrations. Note that the P_O are dominant only at the lowest PO_4 concentrations. Thus, the effects of VarP:N on biological C export is through two factors. It allows P_O to adjust to their nutrient environment but also that it is implemented on a PFT that generally occupies oligotrophic waters causing the variable N:P scheme to increase global C export. The vertical thickness of each color indicates

the relative abundance of the PFT and they are overlaid to sum to one. See Figure S12 for the Control.

VarSi:N improved the simulated surface Si distributions by moving the Si gradient in the SO further south. However, north of 40°S, surface Si concentrations were slightly decreased compared to the *Control*, enhancing the model's widespread underestimation. The largely Fe-limited PI ocean drives higher Si uptake in *VarSi:N*. Notably, areas of *VarSi:N*'s Si underestimation are generally not inhabited with P_{Diat}, and no other simulated PFTs use Si (Gregg & Casey, 2007). The areas of important underestimation are the northwest North Pacific and the Bering Sea, in which P_{Diat} do reside (Figure S3). The persistent nutrient error in this region is attributed to a well-known modeled circulation discrepancy (Kvale et al., 2021; Somes et al., 2017; Weaver et al., 2001).

3.3 Implications of Model Tuning

Preliminary model tuning was performed after *VarP:N* and *VarSi:N* with the intent of improving the accuracy of PI nutrient distributions. Since DOM was overestimated in all experiments, remineralization rates were increased 5-fold (Figure S4). While we note that observations of DOM are spatially limited and carry uncertainty, the increased remineralization rates did reduce the overestimation of the *Control* run to more reasonable values (Figure S4) (Letscher et al., 2013; Mather et al., 2008). After tuning, simulated DOP is slightly underestimated (~0.1 mmol m^{-3}) in the mid-latitude North and South Atlantic, to which the available observations are restricted. DON observations include more data transects in the Indian and Pacific Oceans. DON generally overestimates (~5 mmol m^{-3}) observations slightly in all three ocean basins, except for the SO, where observations are slightly underestimated (~1 mmol m^{-3}). These DON errors should then be considered in our DOC quantifications. These are improvements, nonetheless, to the overestimated DOM values of the *Control*.

Additionally, the preliminary tuning drove slight improvements in inorganic nutrient simulations, making the *Tuned* simulation the most accurate comprehensively (Figures S1 – S3). While tuning does cause a remarkable improvement in simulated O_2 concentrations due to less interior microbial respiration (Figure S7), the simulated interior ocean NO_3 is still too high, although it is reduced relative to *VarP:N* and *VarSi:N*. The upwelling of NO_3 in the SO then

remains elevated above observations (Figure 4B). Tuning restored the PO_4 simulation accuracy to approximately that of the *Control* while retaining the *VarP:N* and *VarSi:N* schemes. There are a few areas of slight PO_4 improvement over the *Control* in the mid-latitudes and the tropics (Figure S2). However, the *Tuned* model did not improve the strength or location of the SO PO_4 gradient. It underestimates the concentrations and places the gradient too far south. The *Control* simulation remains the most accurate in this area.

4. Results

4.1. Changes in Ocean C Storage

Because of more C-laden organic matter and larger total primary producer biomass, the C export out of the euphotic zone into the deep ocean is increased by the VSMs (Table 1, S2, and S3). While each experiment has slightly different global C budgets, a symptom of the PI model spin-up, C inventory differences between them are almost entirely realized within the ocean (Table 2). Thus, our simulated oceans have larger C inventories in PI *VarP:N* and *VarSi:N,* than the *Control*. The *Tuned* model has a slightly smaller inventory caused by the rapid processing of DOC into DIC which then limits ocean C uptake from the PI atmosphere during the spin-up (Figure 6).

Table 1. Global Quantifications.

PI	P_O C:N:P	Export production C:N:P	Carbon export (Pg/yr)	PO_4 export (Pg/yr)
Control	112 : 16 : 1	112 : 16 : 1	8.8	0.62
VarP:N	141 : 20 : 1	130 : 19 : 1	9.4	0.60
VarSi:N	138 : 19 : 1	133 : 19 : 1	9.4	0.60
Tuned	134 : 19 : 1	128 : 18 : 1	9.6	0.64
LGM				
Control	112 : 16 : 1	112 : 16 : 1	7.1	0.50
VarP:N	155 : 22 : 1	141 : 21 : 1	7.7	0.45
VarSi:N	151 : 22 : 1	148 : 21 : 1	8.0	0.44
Tuned	149 : 21 : 1	146 : 21 : 1	8.3	0.46

Note. P_O and EP C:N:P is the globally weighted average. EP C:N:P, C, and P export are calculated from detritus at the base of the euphotic zone (120 m).

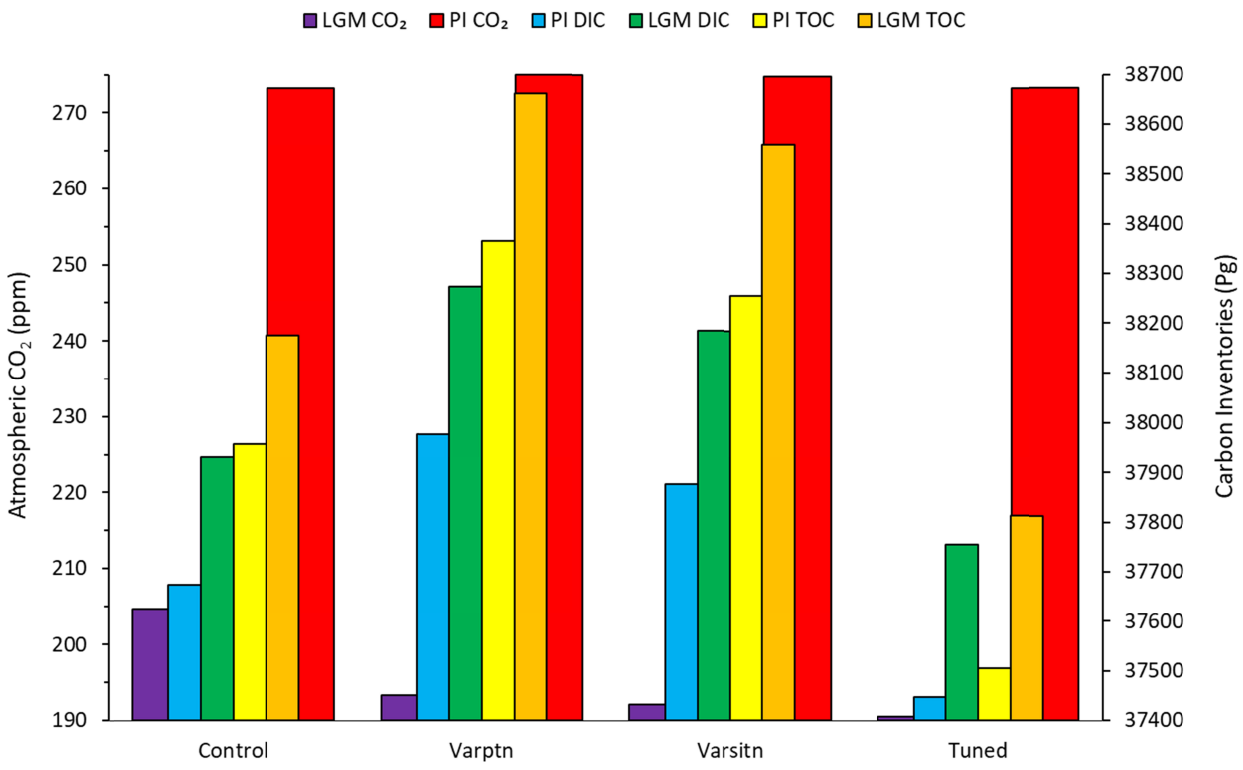

Figure 6. Comparison of pCO_2, DIC, and Total Ocean Carbon inventories in the PI and LGM. The two pCO_2 variables use the left vertical axis, while all others use the right axis. TOC is the sum of DIC, DOC, and POC.

Table 2. Differences in C inventories between models.

	***p*CO₂ (ppm)**	**Ocean total carbon (Pg)**	**Ocean DIC (Pg)**	**Ocean DOC (Pg)**	**DOC:DIC (‰)**	**Land carbon (Pg)**
PI:						
VarP:N – Control	2	410	304	106	2.72	4
VarSi:N – Control	1	299	203	96	2.50	3
Tuned – Control	0	-451	-227	-223	-5.91	0
LGM:						
VarP:N – Control	-11	488	342	146	3.75	-47
VarSi:N – Control	-13	384	253	130	3.37	-52
Tuned – Control	-14	-361	-177	-185	-4.86	-58
LMG-PI:						
Control[a]	-69	218	257	-38	-1.05	-73
VarP:N[a]	-82	296	295	2	-0.02	-122
VarSi:N[a]	-83	303	307	-4	-0.18	-127
Tuned[a]	-83	308	307	1	0.00	-130
VarP:N – Control[b]	-13	78	38	40	1.03	-49
VarSi:N – Control[b]	-14	85	50	34	0.88	-54
Tuned – Control[b]	-14	90	50	39	1.06	-57

Note. The PI is the top section and the LGM is the middle section. The top of the bottom section ([a]) shows how a variable changes between climate states, while below that ([b]) shows the relative difference of those changes. E.g., VarP:N – Control = (VarP:N, LGM – PI) – (Control, LGM – PI). Notable here is that the VSMs manifested their increased LGM C storage through relatively larger increases in their DIC and DOC inventories. See Table S3.

The LGM ocean is more oligotrophic than the preindustrial. This is largely due to slower respiration, driven by cooler temperatures, and a weaker thermohaline circulation, which reduces the nutrient replenishment from upwelling waters (Buchanan et al., 2016; Galbraith & Skinner, 2020; Matsumoto, 2007; Toggweiler, 1999; Yvon-Durocher et al., 2010). Conversely, higher LGM atmospheric dust fluxes yielded more Fe fertilization to primary producers and furthered nutrient consumption (Muglia et al., 2018). Our LGM configuration captures these characteristics which affect stoichiometry, net primary production (NPP), and carbon cycling (Muglia et al., 2018; Somes & Oschlies, 2015). Thus, our VSMs respond interactively to the LGM conditions, producing substantial differences in the C inventories, compared to *Control,* between the LGM and PI (Table 2). The global C budget for each experiment is approximately conserved between the PI and LGM climate states.

The modeled total ocean carbon (TOC) inventory is the summation of DIC, POC, and DOC. Carbon storage increases in the LGM ocean, relative to the PI, are largely realized in the DIC inventories. In the *Control*, the global ocean DIC inventory increases by 257 Pg C (Figure 6, Table 2, and S3), with all other experiments seeing larger (307-295 Pg C) increases. POC decreased in the LGM ocean by 13% in the *Control* and 7% in the VSMs. The smaller POC reductions in the VSMs lead to LGM *VarP:N* boasting 26% more POC over the *Control*. The depression of P_{Diat} in *VarSi:N* weakens this difference to 24% with similar values for the *Tuned* model. Finally, DOC reduced by 13% in the *Control,* but the VSMs are approximately unchanged. The LGM DOC is larger in *VarP:N* (and *VarSi:N*) by 60% (54%) than the *Control*. The *Tuned* model DOC inventory is much smaller than the other models due to the accelerated DOM remineralization, but this is compensated for by having the largest DIC increase from the PI of any experiment.

503 The DOC invariance in the VSMs is driven by their larger LGM biomasses which
504 increase DOC sourcing via mortality (Table S2). By linearizing the DOC source and sink terms,
505 it is shown that the LGM-PI mortality changes (in particular, the P_O mortalities) are positive in
506 these experiments, whereas they are negative in the *Control* (Table S4). This contradicts the
507 temperature influence, wherein, the VSMs have greater LGM-PI temperature reductions and are
508 colder than the *Control* which slows plankton mortality and DOC recycling (sink term) rates.
509 However, the difference in VSM biomass-induced mortality changes compared to the *Control*'s
510 changes is larger than the comparative difference in the temperature influences on mortality
511 (Table S4). Further, while the VSMs' recycling rates do decrease and decrease more than the
512 *Control*, their larger DOC inventories, driven by larger biomasses, overwhelm the temperature-
513 reducing effect. Lastly, the VSMs' DOC:DIC show that DOC increases relatively more than
514 DIC, wherein the *Control* DOC:DIC is 7.4‰ (Table 2). While the ratio decreases for all models
515 in the LGM, from the PI, the VSMs reduce much less than the *Control*, denoting the remarkable
516 importance of DOC change between climate states.

517 Ultimately, the VSMs increase the ocean C storage from the LGM – PI *Control* model
518 with 38 - 50 Pg more DIC and 34 - 40 Pg more DOC (Table 2). Thus, we identify the DOC
519 response as an important, but thus far overlooked in variable stoichiometry modeling studies,
520 biological C storage mechanism. Figure S17 exemplifies these C changes with zonal averaged
521 cross-sections, wherein *VarP:N* DOC increases from the *Control* in the surface layers. Surplus
522 DOC is subsequently transported into the interior at downwelling sites but remains in the upper
523 cell of the overturning circulation while eventually degrading into DIC. Conversely, DIC is
524 relatively increased by *VarP:N* in the deep layers due to increased POC export. SO upwelling
525 draws the increased DIC to the surface where enhanced outgassing can occur, but this is
526 outweighed by the DIC reduction across all other latitudes leading to a net pCO_2 intake. Some
527 relatively reduced DIC is physically transported into the interior with deep water formation, but
528 additions from POC remineralization throughout the water column soon reverse the deficit into a
529 surplus of DIC.

530 The additional surface ocean C fixation and subsequent sequestration aided in further
531 ocean C uptake from the atmospheric and land inventories. *VarP:N* reduced the LGM pCO_2 from
532 204.7 ppm in the *Control* to 193.3 ppm. The reduction was continued by *VarSi:N* and *Tuned* to

192.1 and 190.5 ppm, respectively. From this and the discussed C inventory changes, the variable Si:N scheme and model tuning have notably smaller C cycle impacts than *VarP:N.* Each simulation did not have the same pCO_2 at the end of the respective PI simulation but the *Tuned* model has the largest pCO_2 decrease of 82.8 ppm (see Figure 6 and Table 2). *VarP:N* and *VarSi:N* have 81.6 and 82.6 respectively, while the *Control* has only a 69 ppm reduction. The LGM pCO_2 in the VSMs are notably more consistent with ice core data than in the *Control* (Bereiter et al., 2015; Ivanovic et al., 2016).

Beyond surface C sequestration, the VSMs reduce surface alkalinity slightly through increases in $CaCO_3$ production, via P_O, and N-fixation. Changes in the ocean's pH buffer capacity, as indicated by DIC:alkalinity, may then be partially responsible for the increased drawdown (Egleston et al., 2010). The ratio changes little in the PI between each experiment, but does more so, albeit still meagerly, in the LGM experiments (Table S3). While DIC and alkalinity both slightly reduce in the surface ocean (not shown), surface DIC change is the dominant effect and increases ocean CO_2 ingassing. We do not focus our analysis on this small effect any further though.

The VSMs also restrict the land carbon inventories further than the *Control*. The lower pCO_2 increased the C limitation for terrestrial primary producers and lowered global temperatures (Ciais et al., 2012; Gerhart & Ward, 2010; Harrison & Prentice, 2003; Ödalen et al., 2020; Prentice et al., 2011). The LGM *Control* sees a 73 Pg reduction in the terrestrial carbon inventory, ignoring the ice sheet burial (Table 2 and S3). The VSMs substantially restrict it by a further 67% (i.e., 49 Pg) for the *VarP:N*, 74% for *VarSi:N*, and 78% for the *Tuned* model. These reductions are still smaller than prior estimates and could be caused by UVic's incomplete terrestrial C cycle (Ciais et al., 2012). The TOC inventory increases are then summations of carbon losses in the atmospheric and terrestrial inventories (Figure 6 and Table S3). Although the model's global carbon inventory is not strictly conserved, there is only 1 - 4 Pg of unaccounted for C gain during the LGM simulations, which is four orders of magnitude smaller than the global C inventory.

4.2. Export Production

The variable N:P scheme creates regions of relatively enhanced or degraded carbon fixation by primary producers, which then redefines the spatial distribution of carbon export to the deep ocean. The obvious caveat to this is that the highest primary producer biomasses are generally in the eutrophic regions where the C and N content of P_O is not as large relative to P. In oligotrophic areas, which cover a larger ocean fraction, biomasses are low, although P_O carry more C and N relative to P (Figures S1 and S2). The total effect on global export production (EP) is then determined by the competing effects of these regions (Figure S14). Note that the P_O ratio is different from the C:N:P of EP, which also depends on the stoichiometry of other PFTs (Figures 7 and 8). The efficiency of the global biological C pump, represented by the weighted C:P of EP (equation 3), increases due to PI *VarP:N* by ~18 C units, with small additions from *VarSi:N*, and slight weakening from *Tuned* model due to the eutrophication caused by increased DOM remineralization (Figure 7).

$$C{:}P|_{global\ EP|_{-120m}} = \left[\frac{1}{\int (EP|_{-120m})\ dA} \times \int \left(N{:}P_{EP|_{-120m}} \times EP|_{-120m}\right) dA\right] \times C{:}N \quad (3)$$

The increase in the C pump's efficiency drives more net C export in the VSMs than in the fixed model (Table 1). Even though the *Tuned* C:P indicates a lower efficiency compared to *VarP:N* and *VarSi:N*, the higher nutrient availability supports a larger primary producer biomass (Table S2) and thus a larger C export.

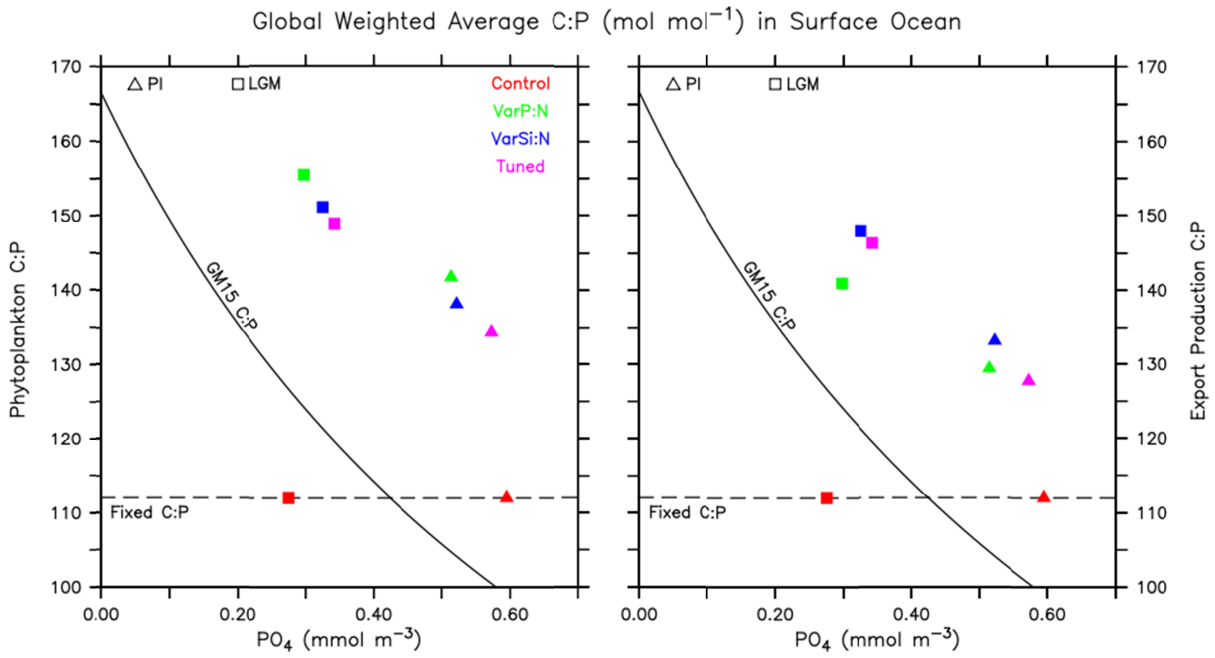

Figure 7. Global weighted average C:P of P_O in the surface ocean (0 – 120 m), left, and EP (at 120 m) which is the weighted C:P contribution of each PFT via the detritus, right. These follow equation 3 methods. The horizontal axis is the unweighted surface average PO_4 that varies slightly between each model due to the perturbations each scheme has on the simulated nutrient cycles.

The VSMs export downward more C per unit P (higher C:N:P) in the relatively oligotrophic LGM ocean than in the PI (Figure 7). Thus, the ocean C inventory increases relative to the LGM *Control*, through larger C EP (Tables 1 and 2). Notably, the P EP is slightly lower in *VarP:N*, in contrast to the C EP, but this does not indicate reduced biology as the P NPP and total biomass increase (Table 3 and S2). *VarP:N* caused a 26% increase in the LGM export C:P relative to the *Control*; *VarSi:N* an additional 5%, with the *Tuned* simulation decreasing it slightly by 1%. While the amount of C exported (Pg year^{-1}) to the deep ocean decreases in all LGM experiments, relative to their PI states, the VSMs show a smaller C export reduction than the LGM-PI *Control* because of the higher C:P's (Table 1). The sluggish ocean overturning counteracts the effects of reduced LGM C exports and increases deep ocean carbon storage (Galbraith & Skinner, 2020; Muglia et al., 2018; Toggweiler, 1999).

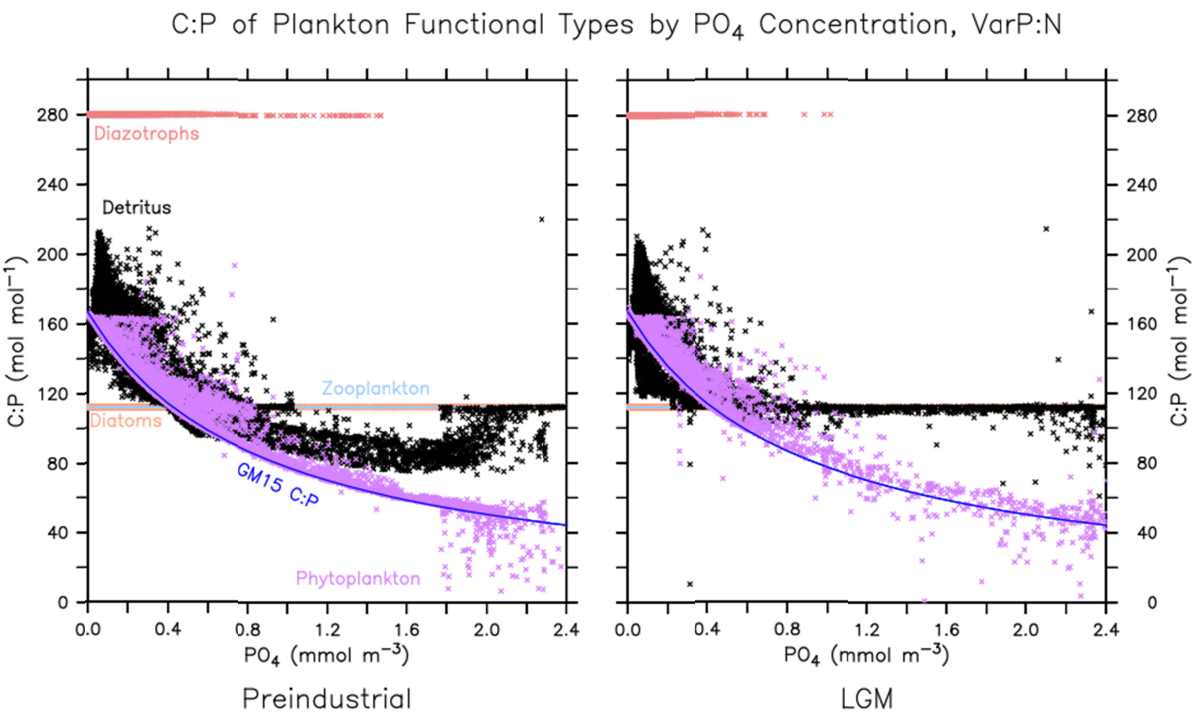

Figure 8. C:P of each PFT across simulated PO_4 concentrations. The detritus relationship is the weighted contribution of each PFT to it. The detritus C:P returns to nearly the Control ratio at high LGM PO_4 due to the significantly lower P_O and P_{Diaz} relative abundance there, Figure 5.

In PI *VarP:N*, zonal weighted average EP C:P, following equation 3, distributions match the configuration of the north and south oligotrophic subtropical gyres with the highest C:N:P between 177–168 : 25–24 : 1 (Figure 9). These ratios are not directly comparable to the weighted P_O C:N:P which is computed over different depths. In the tropics, EP C:N:P in *VarP:N* is depressed to about 124:18:1 by the eutrophic eastern Pacific equatorial upwelling waters. As expected, in the nutrient replete SO, the C:N:P ratios of EP fall below the *Control* value to ~98:14:1 mol/mol (Figure 9). Here, our results are consistent with those of Weber and Deutsch (2010) showing very similar values but *VarP:N*'s latitudinal gradients are slightly sharper (Figure 9). *VarSi:N* and *Tuned* closely match *VarP:N* except for the tropics where the *Tuned* model's greater eutrophy reduces P_O C:N:P as indicated by increases in P_O NPP (Figures 7, 9, and S9). In the LGM ocean, these patterns generally continue, but ratios tend to be higher due to enhanced oligotrophy. Additionally, with the LGM weaker upwelling in the eastern tropical Pacific and the Southern Ocean, the southern subtropical gyre broadens with peak EP C:P values

shifting north. Thus, a spatial expansion of efficient C export occurs there while the northern gyre largely remains unchanged.

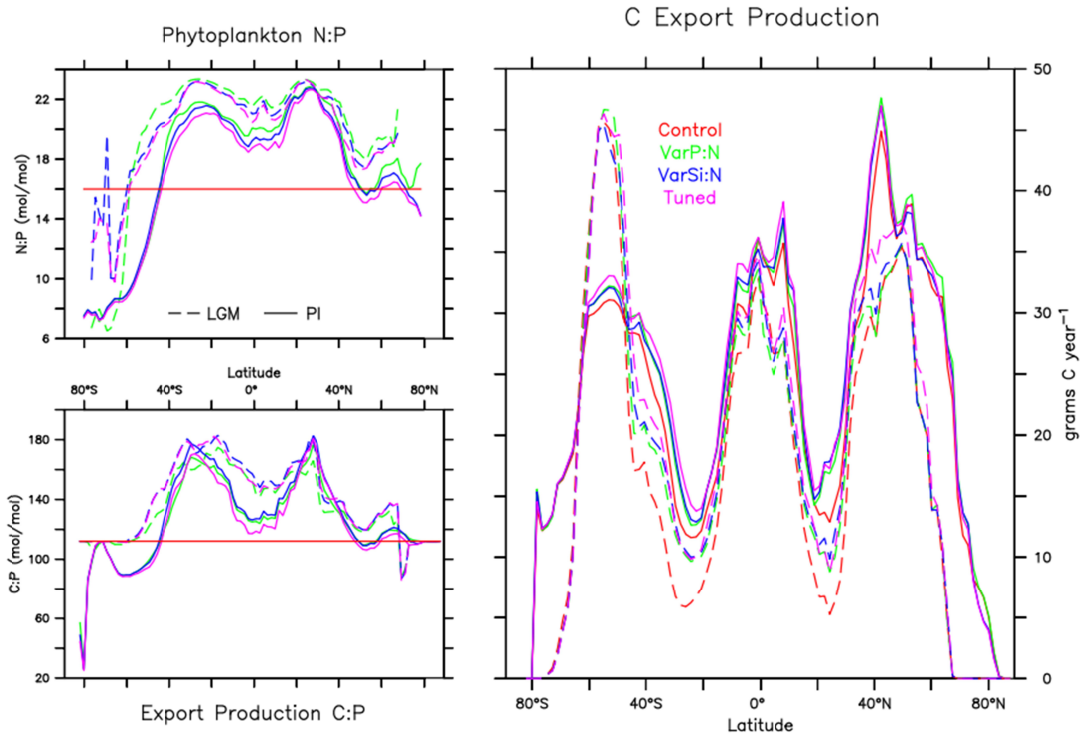

Figure 9. Zonal average P_O N:P weighted by biomass in the surface ocean (0 - 120 m), top left. The bottom left is the same but for EP C:P computed at 120 m. Average C EP is on the right computed at the same level.

Table 3. Globally integrated annual NPP for PI and LGM oceans.

PI	NO_3 NPP (Tmol yr^{-1})	PO_4 NPP (Tmol yr^{-1})	P_O N NPP (Tmol yr^{-1})	P_O P NPP (Tmol yr^{-1})	P_{Diat} N NPP (Tmol yr^{-1})	P_{Diaz} N NPP (Tmol yr^{-1})
Control	754.3	46.5	433.3	27.1	302.5	18.4
VarP:N	853.1	47.3	521.6	27.7	301.6	29.7
VarSi:N	854.9	47.1	642.4	34.9	183.0	29.6
Tuned	873.6	49.8	664.8	37.6	185.5	23.0
LGM						
Control	471.2	29.1	261.7	16.4	199.1	10.4
VarP:N	575.2	29.5	361.1	17.0	191.9	22.4
VarSi:N	583.7	29.5	438.4	21.3	122.8	22.7
Tuned	594.8	30.7	455.4	22.5	123.5	16.0

Note. The P NPP for P_{Diat} and P_{Diaz} are the same as the provided values multiplied by their corresponding fixed P:N (1/16 and 1/40, respectively).

4.3. Primary Producers

Two effects of the VSMs on phytoplankton communities can be distinguished as physiological and taxonomical changes (Matsumoto et al., 2020). Physiological effects arise directly from alterations in the elemental composition of the phytoplankton. However, this also changes the nutrient consumption ratios, which, in the presence of particular nutrient limitations, can alter the competition between the different PFTs. This leads to two PFT, here P_o and $P_{Diaz,}$ cohabitating more harmoniously. Such shifts in the phytoplankton communities are referred to as taxonomic effects. Each of these effects tends to increase the biological C storage. Below, the VSMs' effects are compared to the *Control*, whether PI or LGM, unless explicitly stated otherwise.

4.3.1. Variable P:N Physiological Changes

Due to the plasticity of the P cellular quota in *VarP:N*, P_O inhabiting PO_4 depleted regions are more enriched with N, and thus C, compared to P (Figure 2). Conversely, in PO_4 replete regions, they are less enriched. The global weighted average C:P of P_O, following equation 3, in PI *VarP:N* increased to 141:1 from the *Control*'s 112:1 (Table 1, Figures 7 - 8). This slightly underestimates the global observed mean of 146:1, but it may be due to the model capturing high-latitude eutrophic regions where observations are absent (Martiny et al., 2013). The new C:Ps indicate the larger influence of oligotrophic regions in the global average, which supports a net 7% C export increase. P export, conversely, decreases slightly by 3%. The more oligotrophic LGM exacerbates the N enrichment increasing P_O ratios to 155:1. The depression of P_{Diat} prevalence caused by *VarSi:N* makes more P available and reduces the ratios by 8 and 4 units in the PI and LGM, respectively, but the net C export remained unchanged as P_O grew in their place. Model tuning had a similar effect in the PI and LGM climates where increased retention of N and P in the surface ocean drove slightly reduced C:Ps of 134:1 and 149:1, respectively (Table 1). However, the tuning also supported more total NPP and so the PI and LGM C export increased by an additional 2% and 9 %, respectively, from *VarP:N* (Table 3).

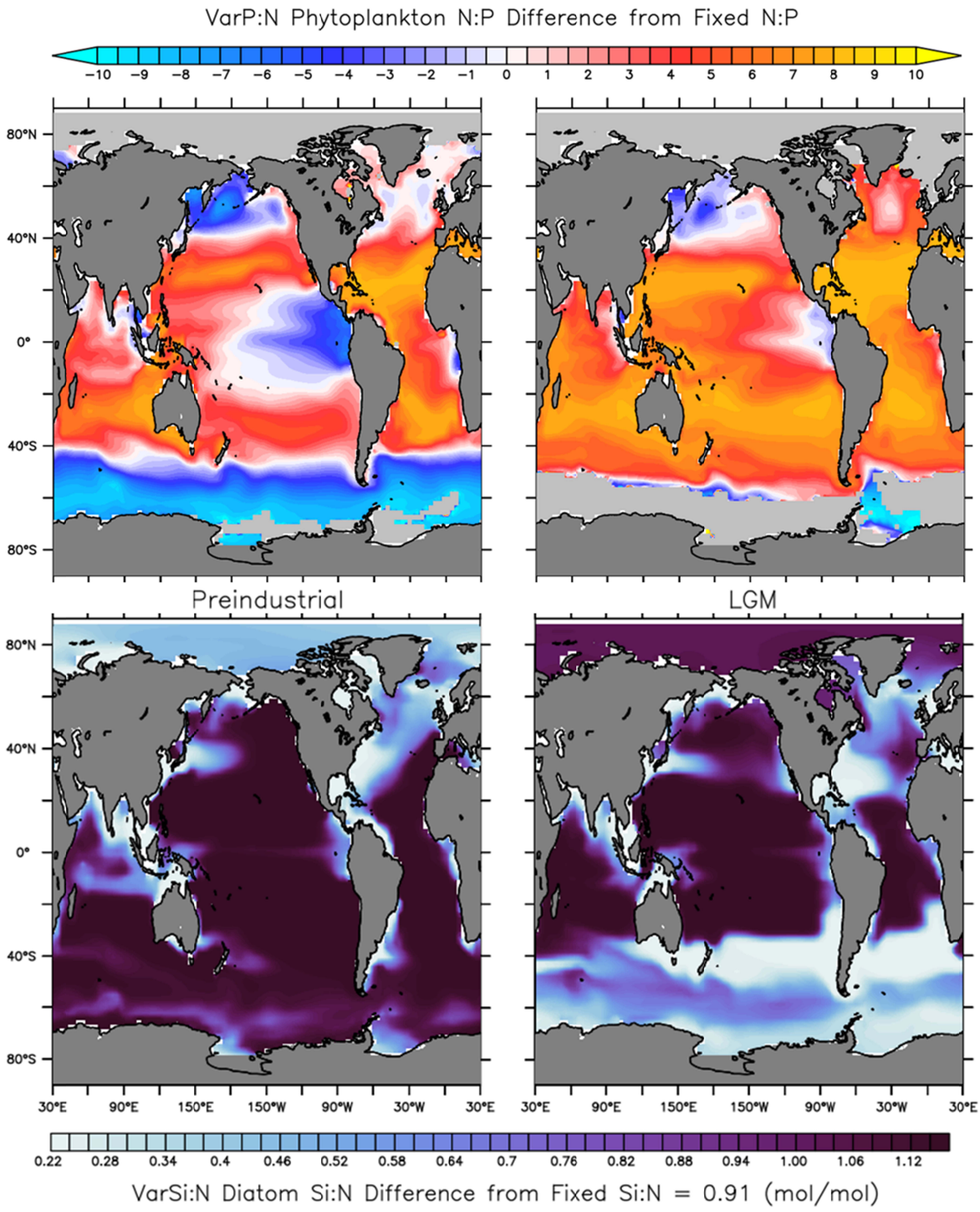

Figure 10. Stoichiometric ratio comparison. Top panels: Difference of P_O N:P under VarP:N as compared to the fixed (Control) ratio (16:1) for the PI (left) and LGM (right) simulations. The light grey colors are erroneous values caused by near-zero P_o concentrations. Bottom panels: Variable P_{Diat} Si:N in the surface ocean (0-120 m) differenced by the fixed Si:N. Light colors

also indicate Fe replete waters nearby the Fe source regions. The dustier LGM climate state is also reflected, bottom right, with more Fe intrusion into the interior basins and the enhanced Fe fertilization occurring in the SO south of 35°S.

P_O N:P in *VarP:N* displays more positive values in the oligotrophic regions and more negative values in eutrophic regions (Figure 10). Via the fixed C:N = 7 relation, the higher N:P regions indicate areas of more efficient carbon fixation, which is communicated to the deep ocean through EP. Zonally averaging these ratios provides a simpler comparison of each experiment. The weighted average N:P of P_O, following equation 3, in the PI surface oligotrophic subtropical gyres display a value of ~ 23-21:1 (C:P = ~ 161-147:1). In the SO eutrophic waters, N:P values fall far below the fixed N:P, as low as 7:1 adjacent to Antarctica (Figure 9).

Most of the PI zonal pattern is carried into the LGM, although south of 20°N the magnitudes increase by 1-6 units in the LGM. The bimodal-like shape is also depressed in LGM *VarP:N* as compared to the PI (Figure 9). The eutrophic upwelling region in the Eastern tropical Pacific is the main cause of the bimodal feature in the PI, driving N:P ratios down. With weaker ocean overturning in the LGM, less PO_4 is upwelled in the eastern tropical Pacific resulting in higher N:P than the PI. In a small region near the most intense LGM upwelling, *VarP:N* ratios still fall below the fixed N:P (Figure 10) but this feature is counterbalanced by higher N:P in the western Pacific and the eastern Atlantic boundary at approximately the same latitudes. The weaker upwelling has the effect of expanding the oligotrophy in the LGM Pacific, thereby expanding the efficiency of the C pump there (i.e., higher C:P), particularly with the subtropical gyres (Figures 9, S15, and S16). The bimodal-like N:P pattern is slightly returned in the *VarSi:N* and *Tuned* experiments. In these runs, slightly more nutritious waters are upwelled in the eastern Pacific driving lower N:P in this latitudinal band (Figure 9).

4.3.2. Variable P:N Taxonomic Shifts

Because Po are almost never P limited, their new P frugality does little to increase their NPP. Their growth is predominantly limited by NO_3 and Fe (Figure 11). P_{Diaz}, however, are generally P limited after Fe and never NO_3 limited. In *VarP:N*, the excess P left behind by P_O fertilizes P_{Diaz}, whose NPP increases by 61% in the PI and 115% in the LGM, consistent with prior research (Table 3) (C. Moore et al., 2013). Notably, the models overestimates prior global

C NPP estimations by ~24 - 14 Pg year^{-1} (Field et al., 1998). The P_o abundance is much larger than P_{Diaz}, which also has a low P requirement (N:P = 40:1) (Figure 5 and S13). Thus, the P transfer to P_{Diaz} is relatively substantial. In turn, P_{Diaz} fix more N_2, if not Fe limited, and over the timescales of biological cycling fertilize the N-limited P_O (Figure 11) (Buchanan et al., 2019a; Capone et al., 2005; Mills & Arrigo, 2010; Wu et al., 2000). P competition between the two still exists, it is simply reduced here, and they still compete for Fe (Somes et al., 2010). The improved P_O-P_{Diaz} cohabitation then supports a larger biomass and biological C pump (Table 1 and S2).

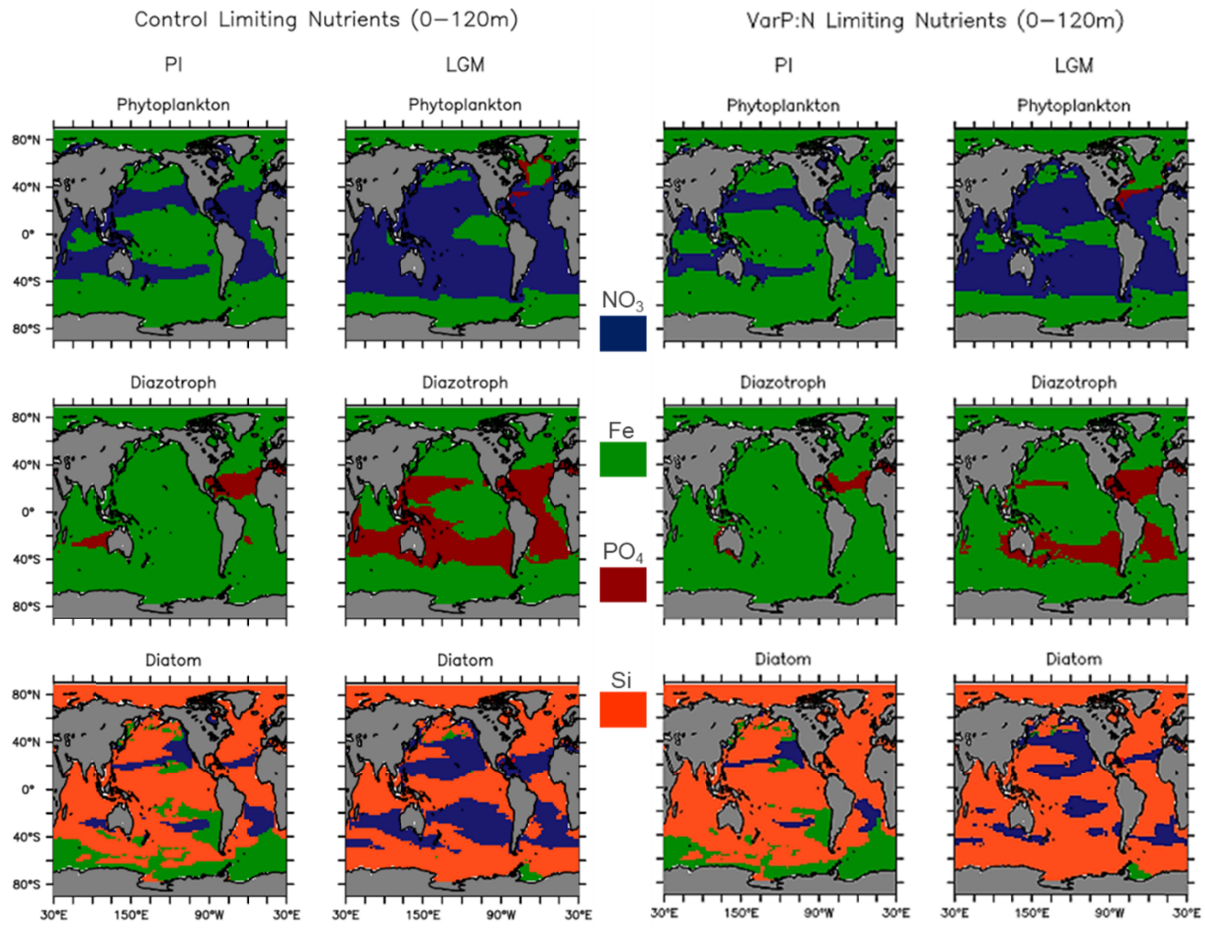

Figure 11. Primary limiting nutrients for each PFT in the surface ocean (0 – 120m). The P_{Diaz} P limitation decreases due to VarP:N while the N limitation decreases for P_o and P_{Diat}. The dustier LGM decreases the Fe limitation for all between the PI and LGM simulations.

Spatially P_{Diaz} NPP/biomass increases correlate well with P_O N NPP/biomass increases which are in the Indonesian archipelago and the tropical/midlatitude western Atlantic (Figure

12). The cohabitation is also visualized with collocated increases in NO_3 and DON (Figures S1 and S4). Finally, the increases in P_{Diaz} NPP, in *VarP:N*, correlate very well with their P limitation from the *Control* (Figure 12) indicating that their P limitation is relieved with *VarP:N*. The exception to this is in the North Atlantic at ~20°N (J. Moore et al., 2004). Here, the P_{Diaz} are still strongly limited by P even after *VarP:N*, consistent with observations (Figure 11) (Wu et al., 2000). In the increased P_O-P_{Diaz} cohabitation regions, there is a mixture of P_{Diat} NPP changes, but these are exceedingly smaller than the increases seen in P_O and P_{Diaz} (Figure 12, S9, and S11). P_{Diat} population size is similar to P_O so the increases in P_O and P_{Diaz} productivity are not likely driven by P_{Diat} population decreases. The reduced P competition between the two PFT is then the most likely driver of the simultaneous growth increases. Additionally, the P_{Diat} N limitation is slightly reduced in P_o-P_{Diaz} improved cohabitation areas (Figure 11). While the N limitation is replaced with a Si limitation, mitigating P_{Diat} growth, the relief still evidences increased P_{Diaz} N-fixation induced by more P availability.

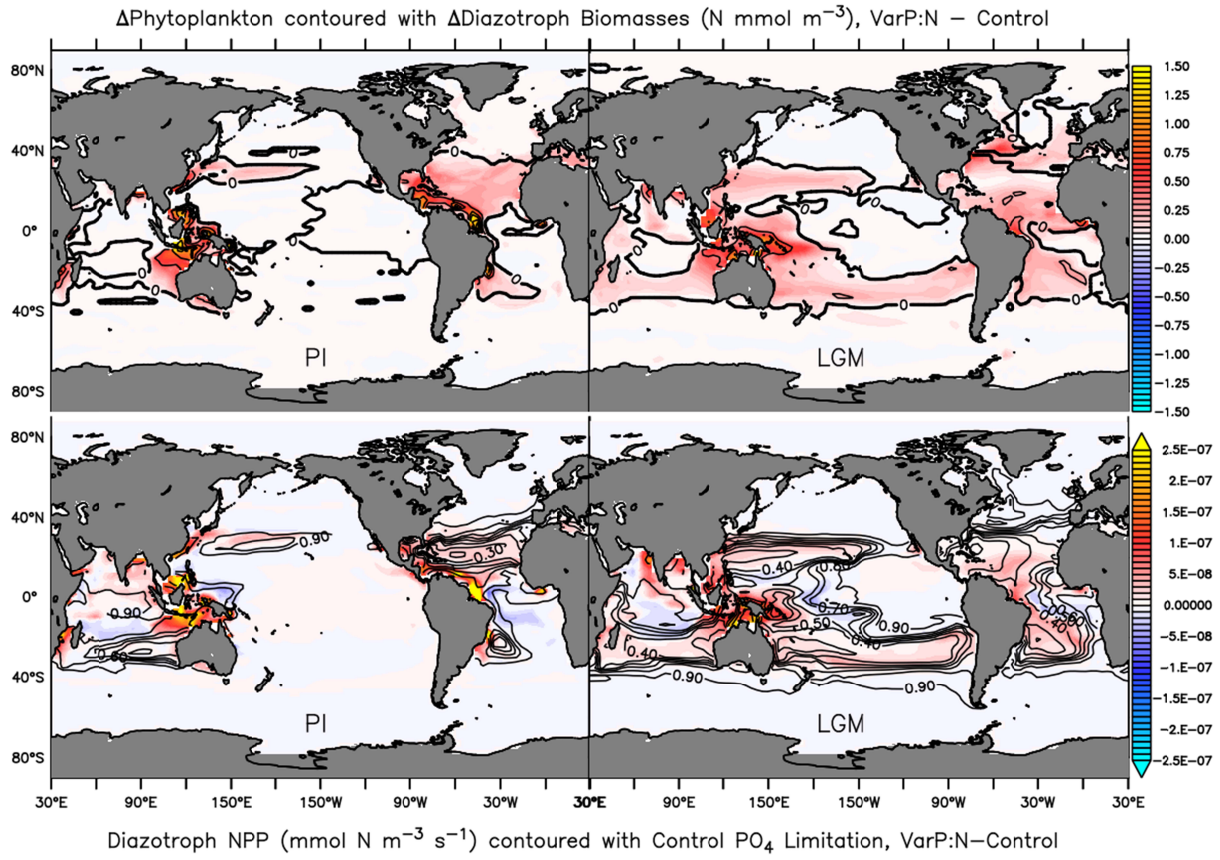

Figure 12. Biomass and growth changes in the surface ocean (0 – 120 m). The left column is PI simulations, and the right is LGM. Top row: The change in P_O biomass between VarP:N and the Control in the surface ocean. Contours of P_{Diaz} biomass changes are overlaid on the same scale, where solid lines indicate positive values. Bottom row: Change in P_{Diaz} NPP between VarP:N and the Control. Contoured lines are P_{Diaz} PO_4 limitation (from 0, meaning complete nutrient limitation, to 1, meaning no nutrient limitation) from the Control. Thus, increases in P_{Diaz} NPP occurring in areas that were previously PO_4 limited indicate where the VarP:N model relieved the PO_4 limitation.

Of course, P_O and P_{Diaz} cohabitate in other regions but the nutrient collaboration may not occur because either the P_{Diaz} are not sufficiently P limited or there is too strong of a Fe limitation for either PFT. E.g., several areas of changing P_O P NPP do not coincide with changes in N NPP, namely the tropical eastern Pacific cold tongue and the Indian Ocean, (Figure S9). In these areas, the P NPP changes in response to equation 1, however, the N NPP remains nearly unchanged because P_O and P_{Diaz} are predominantly limited by Fe (Figures 10 and 11) (Wu et al., 2000). P_O consume Fe faster than the P_{Diaz}, which grow slower, leaving them Fe limited and suppressing the usual cohabitation (Großkopf and LaRoche, 2012; Meyer et al., 2016; Tyrrell, 1999; Ward et al., 2013). Similar behavior continues in the *VarSi:N* and *Tuned* experiments.

The LGM *VarP:N* also incited regions of improved cohabitation, increasing NPP totals (Table 3). In the more oligotrophic LGM ocean, lower PO_4 concentrations initially made P_{Diaz} more P limited than in the PI *Control* but the frugal P_O P consumption in *VarP:N* still substantially relieved the limitation (Figure 11). The response is also aided by the increased LGM Fe fertilization (Buchanan et al., 2019a). The spatial extent of the LGM cohabitation exceeds that seen in the PI ocean but is generally bound to regions where P_{Diaz} are not Fe limited (Figures 11 and 12). Compared to the PI, LGM P_O and P_{Diaz} NPP increases extend far into the Pacific subtropical gyres and dominate most of the Atlantic (Figure 12).

The *VarP:N* model, then, prevents the N NPP reductions seen in the *Control* simulation between the LGM and PI climate states. The higher LGM Fe dust fluxes relieve P_{Diaz} Fe limitation (Figure 11), increasing N-fixation to nearly PI values (Table 4) (Buchanan et al., 2019a). N NPP is then reduced (LGM to PI) by only 32-33% for the VSMs, compared to the

737 *Control*'s 38% reduction. The LGM-PI P NPP reduction was approximately equal across all
738 experiments, indicating more C-laden organic material.

739 **Table 4.** Global N and P inventories and fluxes.

PI:	Surface NO_3 ($\times 10^4$ Tg)	Total NO_3 ($\times 10^6$ Tg)	Surface PO_4 ($\times 10^4$ Tg)	N-fixation (Tg yr^{-1})	Water column denitrification (Tg yr^{-1})	Benthic denitrification (Tg yr^{-1})
Control	1.6	2.7	0.2	256.6	149.9	102.8
VarP:N	2.0	3.1	0.2	414.7	279.3	129.4
VarSi:N	2.2	3.2	0.2	412.7	275.2	130.7
Tuned	2.1	2.8	0.2	320.7	195.9	121.5
LGM:						
Control	0.9	2.6	0.1	145.9	92.6	66.5
VarP:N	1.1	2.6	0.1	313.6	267.6	86.8
VarSi:N	1.2	2.7	0.1	318.2	271.9	89.6
Tuned	1.3	2.9	0.1	224.3	155.4	86.3

740 The accelerated DON remineralization in the *Tuned* model, which causes higher net P_O P
741 consumption, tempers the improved P_O-P_{Diaz} cohabitation but it is mainly at the expense of P_{Diaz}
742 whose original growth is reduced by ~36 and 61% in the PI and LGM, respectively (Table 3).
743 The surface *Tuned* DOP inventory is smaller with little change to the PO_4 inventory, leading to a
744 P_{Diaz} NPP reduction from an increased P limitation and returning it to near *Control* values (Table
745 4 and Figure S8). Conversely, P_O N and P NPP increases between 33 and 36% in both *Tuned*
746 climate states.

747 **4.3.3. Variable P:N N Cycle Changes**

748 The improved P_O-P_{Diaz} cohabitation strongly impacted the global N cycle. Increased P_{Diaz}
749 in *VarP:N* accelerates PI N-fixation by 62% which increased total N NPP and primary producer
750 biomass by 13% and 16%, respectively (Table 4, S2, and S3). The resulting increase in export
751 and remineralization of organic matter causes more deoxygenation and increased water column
752 denitrification by 86%, mainly in the Pacific and Indian Oceans (Table 4 and Figure S22).
753 Smaller increases (26%) occurred in benthic denitrification. While these lead to only a 15%
754 increase in the global NO_3 inventory, the NO_3 of the euphotic zone increased by 25%, thus
755 providing N limitation relief. P_{Diat}'s Si limitation largely limits their response to the excess N and
756 so mainly P_O N NPP increases by 20% globally, with little change in their P NPP (Table 3). This
757 cohabitation-induced N-fixation thus supports more P_O with flexible stoichiometry and enhances
758 C EP.

759 The increased P_{Diaz} activity induced by *VarP:N* altered the LGM NO_3 budget even more
760 than the PI. Globally, N-fixation increased by ~115% compared to the *Control* (Table 4). The
761 resulting NPP and EP increase caused further depletion of oxygen at depth where organic
762 material is respired (Figure S7). The lower O_2 levels are particularly important in the North
763 Pacific, where they crossed the denitrification threshold. *VarP:N*, consequently, causes an
764 increase in denitrification in the LGM (Figure S25) which counteracts the N-fixation increase
765 (Somes et al., 2010). Water column denitrification increased by 189% from the LGM *Control*,
766 much more than in the PI (Table 4 and Figure S22). Benthic denitrification showed a similar
767 increase as the PI of 30%. Even with the widespread expansion of P_{Diaz} and their N-fixation, the
768 global LGM *VarP:N* N inventory slightly decreased by ~ 0.7% from the LGM *Control*. In the
769 euphotic zone, however, the NO_3 inventory increased by 27%, slightly higher than the PI
770 changes.

771 The *Tuned* model reduced N-fixation and denitrification from the *VarP:N* by the
772 accelerated remineralization of DON, which fertilizes the P_O further than P_{Diaz}-sourced N alone.
773 The increased P_O growth in *Tuned* reduces PO_4 availability for P_{Diaz}, whose NPP and N-fixation
774 drop by 22% in the PI. However, the *Tuned* simulation still has 25, 31, and 18% larger N
775 fixation, water column, and benthic denitrification, respectively, compared to the *Control*
776 simulation (Table 4). Thus, the global and surface ocean NO_3 inventories are larger than the
777 *Control* and similar to *VarP:N*. This pattern continues into the LGM but the above numbers are
778 roughly doubled. The *Tuned* LGM NO_3 budget is then slightly larger (12%) than in LGM
779 *VarP:N*, while in the PI it was slightly smaller. The *Tuned* model slightly reduces the total
780 primary producer biomass but it increases the prevalence of flexible stoichiometry P_O, which
781 ultimately yields more C EP. While NPP generally decreased during the LGM relative to the PI
782 (Table 3), variable N:P allows phytoplankton communities to better adapt to the oligotrophic
783 LGM conditions.

784 **4.3.4. Variable Si:N**

785 In *VarSi:N*, P_{Diat} are enriched in Si relative to N in Fe-limited areas and depleted in Si in
786 high-Fe areas, per equation 2. This relation is especially important in the largely Fe-limited PI
787 ocean, Figure 10. *VarSi:N* increases P_{Diat} Si limitation and decreases their global NPP and
788 biomass by about 39% (Table 3, S2, and Figure 11 versus S8). In the LGM, *VarSi:N* causes a

36% reduction despite the increased LGM dust fertilization supplying additional Fe to the surface ocean and lessening the P_{Diat} Si requirement (Conway et al., 2015; Lambert et al., 2015; Muglia et al., 2017, 2018). Note, even at the highest Fe concentrations, *VarSi:N* dictates a higher Si:N than the fixed Si:N scheme (Figures 2 and 12).

With P_{Diat} as a smaller component of the global plankton community, P_O grow in their place. The P_O thus see an increase of ~12% in relative abundance, and a 23% (26%) increase in N (P) NPP, whereas P_{Diaz} changes are small (Table 3 and Table S2). LGM *VarSi:N* leads to a similar 21% (25%) increase in P_O N (P) NPP. The increased PO_4 availability from the reduced P_{Diat} presence decreases the P_O C:P by 8 in the PI and 4 in the LGM, but this has a small effect on the C EP in either climate state (Table 1 and S2). The C:P of EP changes little in the PI, but in the LGM it increases by 7 due to *VarSi:N*. This occurs, counter to the C:P of P_O, because less P_{Diat}, which have C:P of 112:1, exist to be exported. Instead, more P_O with flexible C:P are exported and their ratios are generally higher than 112:1. The primary advantage of the variable Si:N scheme is in constraining the Si and P_{Diat} simulations, but does not have as large of a C cycle influence as *VarP:N*.

Fe-replete waters are generally along the continental margins and P_{Diat} Si:N values are low and approach the fixed Si:N prescribed in the *Control* and *VarP:N* simulations (Figure 10). However, most of the PI ocean is Fe limited, driving high Si:N values and causing enhanced Si consumption of the already limited Si (Figures 11 and S8). Thus, P_{Diat} growth is inhibited, and only P_O grow in their place since P_{Diaz} is slower growing than P_O (Table S2, Figures S11 and S13). The trade-off between P_{Diat} and P_O is clearly seen in zonal plots of each PFTs relative abundance in the plankton community. I.e., where P_{Diat} prevalence decreases, P_o increase. These are also areas of PO_4 concentrations below 1 mmol m^{-3}, indicating that *VarSi:N* has a larger influence on communities in oligotrophic regions (Figures 4 and 5). The more available nutrients induced by *VarSi:N* are not reflected in the nutrient plots due to immediate P_O consumption but they cause a decrease in the P_O C:N:P ratios between 20° and 40°S in the PI and LGM oceans. This is the northernmost extent of the surface Si gradient in the *Control*, which, after *VarSi:N,* is moved south.

With the exception of the higher southern latitudes, P_{Diat} Si:N values are mostly unchanged between the PI and LGM. South of 35°S, enhanced dust Fe fluxes decrease Si:N values to a minimum, which should allow more P_{Diat} NPP than is seen in the PI (Figure S11) (Conway et al., 2015; Muglia et al., 2018). However, the reduced surface Si in the LGM (Table S5), paired with more extensive sea ice, which encroaches into the primary P_{Diat} habitat (Figure S13, PI versus LGM for the green P_{Diat} curve), reduces SO P_{Diat} and negates the effects of a reduced LGM Si requirement caused by higher Fe fluxes. Thus, in the PI P_{Diat} NPP remains largely unaffected by *VarSi:N* in the SO but in the LGM it decreases.

VarSi:N and *Tuned* support the Silicic Acid Leakage Hypothesis (SALH) where during the LGM excess Si escapes the SO via surface waters, subducts into mode waters, and resurfaces in the equatorial East Pacific (Brzezinski et al., 2002; Holzer et al., 2019; Matsumoto et al., 2002, 2014). Figure S18 (A and B) accordingly, show *VarSi:N*'s transport of this relatively increased Si, compared to *VarP:N*. The SALH postulates that, in response, more siliceous phytoplankton grow in the Pacific, displacing other PFT (Figure S18, D). Decreases in the $CaCO_3$:POC export denote the taxonomic shift there from calcifiers (included in P_o) to P_{Diat} (Figure S18, C) (Holzer et al., 2019; Matsumoto et al., 2014). Globally, *VarSi:N* shows relatively lower P_O biomass in the LGM and relatively more P_{Diat} biomass. Thus, the leakage presumably enhances ocean C uptake and storage by limiting $CaCO_3$ production which increases alkalinity. Our results support this but find that the SALH has a smaller global effect on the LGM ocean C storage than our variable N:P model. *p*CO2 further reduces by only 1 ppm relative to *VarP:N*'s 13 ppm reduction and TOC increases by 7 Pg compared to *VarP:N*'s 78 Pg relative increase (Table 2). *VarSi:N*'s global C export change, 0.3 Pg $year^{-1}$, is larger though compared to *VarP:N*'s zero change (Table 1).

Matsumoto et al. (2014) presented three possible mechanisms to induce the Si leak. They are enhanced SO Fe fertilization decreasing Si:N, more expansive sea ice that limits P_{Diat} growth, and weaker SO overturning that removes SO trapping. Our model includes the enhanced Fe flux and the increased sea ice in the LGM. The SO westerly wind stress is effectively unchanged from the PI, however, confirming their conclusion that it may not be a required trigger (Matsumoto et al., 2014). A detailed investigation of the SALH is beyond this research and we do not investigate the sensitivities or causes therein.

5. Discussion

The ubiquitous fixed phytoplankton stoichiometry assumption has been shown to limit model performance, predominantly through the spatial smoothing of the biological C pump (Matsumoto et al., 2020; Ödalen et al., 2020). The results presented here, among other studies, suggest that the implementation of variable stoichiometry can not only affect the simulations of the biological pump but also the structure of phytoplankton communities through taxonomic shifts and changes in nutrient limitations. Thus, the inclusion of variable stoichiometry in global climate models can enhance ocean C storage through larger DIC and DOC inventories causing a further 13 – 14 ppm drawdown of pCO_2 between the LGM and PI climate states. Per our results, we stress the importance of the DOC inventory response to variable stoichiometry, which has been overlooked previously. While the DOC inventory is much smaller than the DIC, it responds by a similar magnitude as DIC to the GM15 model. In the following section, we compare our results to prior research and find that they are consistent, suggesting that our quantifications of C inventories, fluxes, and changes are reasonable.

From the PI climate state to the LGM, Matsumoto et al.'s (2020) pCO_2 reduced by 34 ppm under fixed C:N:P whereas our results show a 69 ppm reduction that is closely matched by Ödalen et al.'s (2020) 64 ppm reduction. These pCO_2 reductions strongly depend on the configuration of forcing conditions implemented in a given model for LGM simulations (as suggested in section S4). However, the effects of variable stoichiometry on pCO_2 are similar across these studies. Matsumoto et al.'s (2020) GM15 framework was responsible for an additional 11 ppm drawdown and their power law model a 20 ppm drawdown. Ödalen et al.'s GM15 scheme was responsible for a slightly higher reduction of 16 ppm while our schemes vary between 13 and 14 ppm.

The differences in pCO_2 response may partly stem from different biogeochemical simulation methods. For example, MOBI normally, though unrealistically, instantaneously disassociates the P_{Diat}'s soft tissue from their silica frustules and routes it to the detritus inventory, which has a slower sinking velocity (~3 times) than the simulated biogenic silica (Zúñiga et al., 2021). The accelerated sinking of P_{Diat} POM, via silica ballasting, could add ~3.7 to 1.3 Pg C $year^{-1}$ to the deep ocean inventory (section S3.1 and Table S5), and presumably cause

a further 3-6 ppm pCO_2 reduction, putting our model roughly between the power law and GM15 quantifications (Matsumoto et al., 2020; Ödalen et al., 2020, respectively).

5.1. Carbon Export and Ocean Storage

At the PI steady state, the VSMs have higher export C:N:P (Figure 7 and Table 1) than Ödalen et al.'s (2020) C:P of 121:1, who uses GM15 in the model cGENIE. Tanioka & Matsumoto (2017), using a stoichiometric power law for C:P in the MESMO2 model, found a notably lower PI ratio of 103:15:1. In subsequent studies, these authors substantially revised the power law scheme and also tested the GM15 relation in MESMO2 (Matsumoto et al., 2020; Tanioka & Matsumoto, 2020). The new power law produced 113:16:1 and the GM15 scheme 107:16:1.

While Matsumoto et al. (2020) suggest that low export C:N:P in their findings, is driven by the lack of preferential nutrient remineralization, the cGENIE model also carries this simplification but better matches our model, which does include it. Although, the cGENIE and MOBI similarity could be induced by cGENIE only having one PFT, and thus a more expansive application of GM15's variable C:P, which may overcome the lack of preferential nutrient remineralization. Another possibility for the C:P difference between these studies is likely a symptom of GM15 implementation methods, in which Matsumoto et al. (2020) applied it to all PFTs, thus inciting nutrient frugality everywhere, creating an excess of PO_4, and lowering ratios. Finally, the performance of stoichiometric schemes could be sensitive to the differences in simulated biogeochemical processes and inventories between the models. For example, we have shown that the increased P_O-P_{Diaz} cohabitation partly explains the increases in ocean C sequestration in *VarP:N*. However, this process is partly controlled by Fe availability. Thus, when a different LGM sub-grid bathymetry mask adjusts sedimentary Fe fluxes and reduces both the global and euphotic zone Fe inventories, the implications of our VSMs are not as profound (section S4 and Table S6). The biogeochemistry in MESMO2 and cGENIE could be different from MOBI's and so cause the differences in the variable stoichiometry effects. Further testing is needed to discover the sensitivities of any given stoichiometry model to variations in simulated biogeochemical processes and inventories.

904 The LGM climate state, with oligotrophic surface waters, increases the stoichiometric
905 ratios across these studies. *VarP:N* EP C:P increases by 11 C units in the LGM, which is smaller
906 than expected, per equation 1, based on the PO_4 change but is caused by the increased prevalence
907 of fixed stoichiometry PFTs (Figures 5, 7 and Table 1). Matsumoto et al.'s (2020) LGM GM15
908 C:P is substantially lower than ours at 120:1 but their C:P ratios increase by approximately the
909 same magnitude between the PI and LGM as our simulations. Conversely, their power law model
910 induces a 27-unit C:P increase, bringing it to about the same ratio as *VarP:N*. Ödalen et al.'s
911 (2020) LGM GM15 experiment sees a similar increase to *VarP:N* at 13 units. The *VarSi:N* and
912 *Tuned* experiments show increases of 15 and 18 C units, respectively.

913 The EP C:P change consequently alters the POC and POP export. The power law model
914 causes a smaller impact on C export (Matsumoto et al., 2020; Tanioka & Matsumoto, 2017,
915 2020). They found a 0.04 Pg C $year^{-1}$ increase in the PI while our *VarP:N* shows a 0.59 Pg C
916 $year^{-1}$ increase (Table 1) (Tanioka & Matsumoto, 2017). Subsequently, Matsumoto et al.'s (2020)
917 PI C export shows a 0.4 Pg C $year^{-1}$ power law increase and 0.1 Pg C $year^{-1}$ decrease under
918 GM15. The 2020 power law revision brings the two models into much better agreement with
919 respect to absolute numbers, but their usage of GM15 produces a carbon export change, relative
920 to the fixed-ratio simulations, that is of opposite sign to our results. All our simulations are
921 consistent with observation-derived estimations though the range is broad (Boyd & Trull, 2007).
922 Buchanan et al., (2019b) briefly report an increase of 0.4 Pg yr^{-1} in PI C EP due to GM15 in the
923 CSIRO model.

924 From the PI to LGM, the *Control* POC and POP reduce by the same 19% (Table 1).
925 However, in *VarP:N*, the POP export reduced by 26% while the POC export only reduced by
926 17.6%. Thus, sinking organic particles are more carbon-laden and the biological C pump is more
927 efficient under *VarP:N* than the *Control*. Our remaining experiments, *VarSi:N* and *Tuned*, do not
928 substantially alter these results. Ödalen et al.'s (2020) GM15 scheme reports a similar LGM POC
929 export decrease, relative to the PI, of 5% less than their fixed stoichiometry simulation and 2%
930 larger of a POP decrease. Matsumoto et al.'s (2020) GM15 showed the same POC export
931 reduction but with a 5% larger POP reduction. Alternatively, under the power law, the POP
932 reduced by a further 6%, compared to a fixed ratio simulation, and the POC export reduction was
933 12% less. Thus, the biological pump responds similarly across three different climate models if

the GM15 scheme is implemented contrary to the notably different C:Ps. Matsumoto et al.'s (2020) annual C export decreases (LGM - PI) between 0.5 (power law), 1.1 (GM15), and 1.6 Pg C yr^{-1} (fixed), compared to 1.4 Pg C yr^{-1} in our *Tuned* model and 1.7 Pg C yr^{-1} in our *Control* experiment. Their GM15 LGM C EP quantification is very similar to our results, yet their power law model changes little and is closer to our PI C EP (Table 1). Ödalen et al. (2020) did not report any C export quantifications.

With the similarities of our findings to other studies which use unique ocean biogeochemical and climate models, the quantifications of the biological carbon pump and the effects of including realistic variable stoichiometry presented here are reasonable and likely good approximations in the LGM climate. While our model carries some limitations and approximations, we have exemplified how the configuration of a model's biogeochemistry may influence these quantifications of the biological C pump and the effects variable stoichiometric schemes may have on it. Further research on the sensitivities of variable stoichiometry schemes to various biogeochemical processes is needed.

6. Conclusions

Variable stoichiometry schemes allow simulated primary producers to adapt to a variety of nutrient environments consistent with observations. The variable N:P scheme implemented in our ocean biogeochemistry model allowed P_O to exhibit P flexibility as the ambient PO_4 concentration varies. The P flexibility has two important consequences. First, the P_O P limitation is reduced, allowing them to grow more in low-PO_4 environments, fix more C there, and become relatively more C-laden. Second, the P_O PO_4 frugalness stokes an ecological response via increased PO_4 availability for P_{Diaz}, leading to an improved cohabitation between P_O and P_{Diaz}, more net N and C fixation, and higher net C EP. The first consequence describes how N:P flexibility enhances the biological C pump's efficiency (i.e., more C export per P), and the second, how it can strengthen of the biological C pump by supporting a larger primary producer biomass. While the variable Si:N scheme did not show the same strong influence over the C pump, it does showcase how realistic modeling of nutrient quota ratios may improve representations of biogeochemical cycles.

The LGM experiments suggest that the new nutrient flexibility allows the formation of diverse phytoplankton communities, more responsive and interactive ocean biogeochemical cycles, and increased ocean carbon storage with lower pCO_2. Our results, in addition to other studies, then suggest that the robustness of model performance in various climate states may depend, at least in part, on capturing the variability of ocean primary producers and their community structures. We find that capturing these attributes leads to 78 – 90 Pg more ocean carbon storage, realized through both the DIC and DOC inventories, in the LGM ocean as compared to fixed stoichiometry. We identify the DOC response as a significant but previously overlooked C storage mechanism in this context. Increased ocean C storage, thus, causes pCO_2 to be 13 – 14 ppm lower in the VSMs. Variable stoichiometry may then explain a notable portion of the pCO_2 difference between the PI and LGM climates while unveiling important mechanisms within primary producer communities and biogeochemical cycles that partly define the ocean carbon cycle.

Acknowledgments

This work was supported by the National Science Foundation (grant #1924215). Model data processing, analysis, imaging, and computational actions were performed using NOAA's Pacific Marine Environmental Laboratory products Ferret and PyFerret software (http://ferret.pmel.noaa.gov/Ferret/). Microsoft PowerPoint was also used in some imaging (Microsoft Corporation, 2018). Nate Fillman is appreciative of Burke Hales, Samar Khatiwala, and Alan Mix for their helpful comments and discussions throughout this work.

Open Research

Model code is publicly accessible at https://github.com/fillmann/variable-stoichiometry. Model output, initialization and forcing data, simulation control, and restart files are publicly available at https://doi.org/10.5281/zenodo.8161356.

References

Aumont, O., Maier-Reimer, E., Blain, S., & Monfray, P. (2003). An ecosystem model of the global ocean including Fe, Si, P colimitations: An ecosystem model of the world ocean. *Global Biogeochemical Cycles*, *17*(2). https://doi.org/10.1029/2001GB001745

Barnola, J. M., Raynaud, D., Korotkevicht, Y. S., & Lorius, C. (1987). Vostok ice core provides 160,000-year record of atmospheric CO_2. *Nature*, 329(6138), 408–408.

Bauska, T. K., Joos, F., Mix, A. C., Roth, R., Ahn, J., & Brook, E. J. (2015). Links between atmospheric carbon dioxide, the land carbon reservoir and climate over the past millennium. *Nature Geoscience*, *8*(5), 383–387. https://doi.org/10.1038/ngeo2422

Bereiter, B., Eggleston, S., Schmitt, J., Nehrbass-Ahles, C., Stocker, T. F., Fischer, H., et al. (2015). Revision of the EPICA Dome C CO_2 record from 800 to 600 kyr before present: Analytical bias in the EDC CO2 record. *Geophysical Research Letters*, *42*(2), 542–549. https://doi.org/10.1002/2014GL061957

Bisson, K., Siegel, D. A., & DeVries, T. (2020). Diagnosing Mechanisms of Ocean Carbon Export in a Satellite-Based Food Web Model. *Frontiers in Marine Science*, *7*, 505. https://doi.org/10.3389/fmars.2020.00505

Bouttes, N., Paillard, D., Roche, D. M., Brovkin, V., & Bopp, L. (2011). Last Glacial Maximum CO_2 and $\delta^{13}C$ successfully reconciled. *Geophysical Research Letters*, *38*. https://doi.org/10.1029/2010GL044499

Boyd, P. W., & Trull, T. W. (2007). Understanding the export of biogenic particles in oceanic waters: Is there consensus? *Progress in Oceanography*, *72*(4), 276–312. https://doi.org/10.1016/j.pocean.2006.10.007

Brovkin, V., Ganopolski, A., Archer, D., & Rahmstorf, S. (2007). Lowering of glacial atmospheric CO_2 in response to changes in oceanic circulation and marine biogeochemistry. *Paleoceanography*, *22*(4). https://doi.org/10.1029/2006PA001380

Brzezinski, M.A., Pride, C. J., Franck, V. M., Sigman, D. M., Sarmiento, J. L., Matsumoto, K., et al. (2002). A switch from $Si(OH)_4$ to NO_3^- depletion in the glacial Southern Ocean. *Geophysical Research Letters*, *29*(12), 5–1–5–4. https://doi.org/10.1029/2001GL014349

Buchanan, P. J., Chase, Z., Matear, R. J., Phipps, S. J., & Bindoff, N. L. (2019a). Marine nitrogen fixers mediate a low latitude pathway for atmospheric CO_2 drawdown. *Nature Communications*, *10*(1), 4611. https://doi.org/10.1038/s41467-019-12549-z

Buchanan, P. J., Matear, R. J., Chase, Z., Phipps, S. J., & Bindoff, N. L. (2019b). Ocean carbon and nitrogen isotopes in CSIRO Mk3L-COAL version 1.0: A tool for palaeoceanographic research. *Geoscientific Model Development*, *12*(4), 1491–1523. https://doi.org/10.5194/gmd-12-1491-2019

Buchanan, P. J., Matear, R. J., Lenton, A., Phipps, S. J., Chase, Z., & Etheridge, D. M. (2016). The simulated climate of the Last Glacial Maximum and insights into the global marine carbon cycle. *Climate of the Past*, *12*(12), 2271–2295. https://doi.org/10.5194/cp-12-2271-2016

Capone, D. G., Burns, J. A., Montoya, J. P., Subramaniam, A., Mahaffey, C., Gunderson, T., et al. (2005). Nitrogen fixation by *Trichodesmium* spp.: An important source of new nitrogen to the tropical and subtropical North Atlantic Ocean *Global Biogeochemical Cycles*, *19*(2). https://doi.org/10.1029/2004GB002331

Ciais, P., Tagliabue, A., Cuntz, M., Bopp, L., Scholze, M., Hoffmann, et al. (2012). Large inert carbon pool in the terrestrial biosphere during the Last Glacial Maximum. *Nature Geoscience*, *5*(1), 74–79. https://doi.org/10.1038/ngeo1324

Clark, L. L., Ingall, E. D., & Benner, R. (1998). Marine phosphorus is selectively remineralized. *Nature*, *393*(6684), 426–426. https://doi.org/10.1038/30881

Conway, T. M., Wolff, E. W., Röthlisberger, R., Mulvaney, R., & Elderfield, H. E. (2015). Constraints on soluble aerosol iron flux to the Southern Ocean at the Last Glacial Maximum. *Nature Communications*, *6*(1), 7850. https://doi.org/10.1038/ncomms8850

Cox, P.M. (2001). Description of the "TRIFFID" dynamic global vegetation model. Hadley Centre, Met Office, UK. https://jules.jchmr.org/sites/default/files/HCTN_24.pdf

Du, J., Haley, B. A., & Mix, A. C. (2020). Evolution of the Global Overturning Circulation since the Last Glacial Maximum based on marine authigenic neodymium isotopes. *Quaternary Science Reviews*, *241*, 106396. https://doi.org/10.1016/j.quascirev.2020.106396

Egleston, E. S., Sabine, C. L., & Morel, F. M. M. (2010). Revelle revisited: Buffer factors that quantify the response of ocean chemistry to changes in DIC and alkalinity. *Global Biogeochemical Cycles*, *24*(1). https://doi.org/10.1029/2008GB003407

Falkowski, P. (2012). The power of plankton. *Nature*, *483*(7387), S17-S20

Field, C. B., Behrenfeld, M. J., Randerson, J. T., & Falkowski, P. (1998). Primary Production of the Biosphere: Integrating Terrestrial and Oceanic Components. *Science*, *281*(5374), 237–240. https://doi.org/10.1126/science.281.5374.237

Flynn, K. J. (2010). Ecological modelling in a sea of variable stoichiometry: Dysfunctionality and the legacy of Redfield and Monod. *Progress in Oceanography*, *84*(1–2), 52–65. https://doi.org/10.1016/j.pocean.2009.09.006

Franck, V. M., Brzezinski, M. A., Coale, K. H., & Nelson, D. M. (2000). Iron and silicic acid concentrations regulate Si uptake north and south of the Polar Frontal Zone in the Pacific Sector of the Southern Ocean. *Deep-Sea Research II*, *47*(15-16), 3315-3338. https://doi.org/10.1016/S0967-0645(00)00070-9

Galbraith, E. D., Gnanadesikan, A., Dunne, J. P., & Hiscock, M. R. (2010). Regional impacts of iron-light colimitation in a global biogeochemical model. *Biogeosciences*, *7*(3), 1043-1064. https://doi.org/10.5194/bg-7-1043-2010

Galbraith, E. D., Kienast, M., & The NICOPP working group members. (2013). The acceleration of oceanic denitrification during deglacial warming. *Nature Geoscience*, *6*(7), 579–584. https://doi.org/10.1038/ngeo1832

Galbraith, E. D., & Martiny, A. C. (2015). A simple nutrient-dependence mechanism for predicting the stoichiometry of marine ecosystems. *Proceedings of the National Academy of Sciences*, *112*(27), 8199–8204. https://doi.org/10.1073/pnas.1423917112

Galbraith, E. D., & Skinner, L. C. (2020). The Biological Pump During the Last Glacial Maximum. *Annual Review of Marine Science*, *12*(1), 559–586. https://doi.org/10.1146/annurev-marine-010419-010906

Garcia, C. A., Baer, S. E., Garcia, N. S., Rauschenberg, S., Twining, B. S., Lomas, M. W., & Martiny, A. C. (2018). Nutrient supply controls particulate elemental concentrations and ratios in the low latitude eastern Indian Ocean. *Nature Communications*, *9*(1), 4868. https://doi.org/10.1038/s41467-018-06892-w

Garcia, H. E., Locarnini, R. A., Boyer, T. P., Antonov, J. I., Baranova, O. K., Zweng, M. M., et al. (2013). World Ocean Atlas 2013. Volume 4, Dissolved inorganic nutrients (phosphate, nitrate, silicate). *NOAA Atlas NESDIS 76,* https://doi.org/10.7289/V5J67DWD

Garcia, N. S., Sexton, J., Riggins, T., Brown, J., Lomas, M. W., & Martiny, A. C. (2018). High Variability in Cellular Stoichiometry of Carbon, Nitrogen, and Phosphorus Within Classes of Marine Eukaryotic Phytoplankton Under Sufficient Nutrient Conditions. *Frontiers in Microbiology*, *9*, 543. https://doi.org/10.3389/fmicb.2018.00543

Geider, R., & La Roche, J. (2002). Redfield revisited: Variability of C:N:P in marine microalgae and its biochemical basis. *European Journal of Phycology*, *37*(1), 1–17. https://doi.org/10.1017/S0967026201003456

Gerhart, L. M., & Ward, J. K. (2010). Plant responses to low [CO_2] of the past. *New Phytologist*, *188*(3), 674–695. https://doi.org/10.1111/j.1469-8137.2010.03441.x

Gregg, W. W., & Casey, N. W. (2007). Modeling coccolithophores in the global oceans. *Deep Sea Research Part II: Topical Studies in Oceanography*, *54*(5–7), 447–477. https://doi.org/10.1016/j.dsr2.2006.12.007

Großkopf, T., & LaRoche, J. (2012). Direct and indirect costs of dinitrogen fixation in *Crocosphaera watsonii* WH8501 and possible implications for the nitrogen cycle. *Frontiers in Microbiology*, *3*. https://doi.org/10.3389/fmicb.2012.00236

Gruber, N., & Sarmiento, J. L. (1997). Global patterns of marine nitrogen fixation and denitrification. *Global Biogeochemical Cycles*, *11*(2), 235–266. https://doi.org/10.1029/97GB00077

Harrison, S. P., & Prentice, C. I. (2003). Climate and CO_2 controls on global vegetation distribution at the last glacial maximum: Analysis based on palaeovegetation data, biome modelling and palaeoclimate simulations. *Global Change Biology*, *9*(7), 983–1004. https://doi.org/10.1046/j.1365-2486.2003.00640.x

Hildebrand, M., & Lerch, S. J. L. (2015). Diatom silica biomineralization: Parallel development of approaches and understanding. *Seminars in Cell & Developmental Biology*, *46*, 27–35. https://doi.org/10.1016/j.semcdb.2015.06.007

Ho, P., Chang, C., Shiah, F., Wang, P., Hsieh, C., & Andersen, K. H. (2020). Body Size, Light Intensity, and Nutrient Supply Determine Plankton Stoichiometry in Mixotrophic Plankton Food Webs. *The American Naturalist*, *195*(4), E100–E111. https://doi.org/10.1086/707394

Holzer, M., Pasquier, B., DeVries, T., & Brzezinski, M. A. (2019). Diatom physiology controls silicic acid leakage in response to iron fertilization. *Global Biogeochemical Cycles*, 33(12), 1631– 1653. https://doi.org/10.1029/2019GB006460

Houghton, R. A. (2007). Balancing the Global Carbon Budget. *Annual Review of Earth and Planetary Sciences*, *35*(1), 313–347. https://doi.org/10.1146/annurev.earth.35.031306.140057

Hutchins, D. A., & Bruland, K. W. (1998). Iron-limited diatom growth and Si:N uptake ratios in a coastal upwelling regime. *Nature*, *393*(6685), 561–564. https://doi.org/10.1038/31203

Inomura, K., Deutsch, C., Jahn, O., Dutkiewicz, S., & Follows, M. J. (2022). Global patterns in marine organic matter stoichiometry driven by phytoplankton ecophysiology. *Nature Geoscience*, *15*(12), 1034–1040. https://doi.org/10.1038/s41561-022-01066-2

Ivanovic, R. F., Gregoire, L. J., Kageyama, M., Roche, D. M., Valdes, P. J., Burke, A., et al. (2016). Transient climate simulations of the deglaciation 21–9 thousand years before present (version 1) – PMIP4 Core experiment design and boundary conditions. *Geoscientific Model Development*, *9*(7), 2563–2587. https://doi.org/10.5194/gmd-9-2563-2016

Jaccard, S. L., & Galbraith, E. D. (2012). Large climate-driven changes of oceanic oxygen concentrations during the last deglaciation. *Nature Geoscience*, *5*(2), 151–156. https://doi.org/10.1038/ngeo1352

Jeltsch-Thommes, A., Battaglia, G., Cartapanis, O., Jaccard, S. L., & Joos, F. (2019). Low terrestrial carbon storage at the Last Glacial Maximum: constraints from multi-proxy data. *Climate of the Past*, *15*(2), 849–879. https://doi.org/10.5194/cp-15-849-2019

Jiao, N., Herndl, G. J., Hansell, D. A., Benner, R., Kattner, G., Wilhelm, S. W., et al. (2010). Microbial production of recalcitrant dissolved organic matter: Long-term carbon storage

in the global ocean. *Nature Reviews Microbiology*, *8*(8), 593–599. https://doi.org/10.1038/nrmicro2386

Kageyama, M., Albani, S., Braconnot, P., Harrison, S. P., Hopcroft, P. O., Ivanovic, R. F., et al. (2017). The PMIP4 contribution to CMIP6 – Part 4: Scientific objectives and experimental design of the PMIP4-CMIP6 Last Glacial Maximum experiments and PMIP4 sensitivity experiments. *Geoscientific Model Development*, *10*(11), 4035–4055. https://doi.org/10.5194/gmd-10-4035-2017

Khatiwala, S., Schmittner, A., & Muglia, J. (2019). Air-sea disequilibrium enhances ocean carbon storage during glacial periods. *Science Advances*, *5*(6), eaaw4981. https://doi.org/10.1126/sciadv.aaw4981

Klausmeier, C. A., Litchman, E., & Levin, S. A. (2004). Phytoplankton growth and stoichiometry under multiple nutrient limitation. *Limnology and Oceanography*, *49*(4, part2), 1463–1470. https://doi.org/10.4319/lo.2004.49.4_part_2.1463

Kohfeld, K. E., Quéré, C. L., Harrison, S. P., & Anderson, R. F. (2005). Role of Marine Biology in Glacial-Interglacial CO_2 Cycles. *Science*, *308*(5718), 74–78. https://doi.org/10.1126/science.1105375

Kvale, K. F., Meissner, K. J., Keller, D. P., Eby, M., & Schmittner, A. (2015). Explicit Planktic Calcifiers in the University of Victoria Earth System Climate Model, Version 2.9. *Atmosphere-Ocean*, *53*(3), 332–350. https://doi.org/10.1080/07055900.2015.1049112

Kvale, K., Keller, D. P., Koeve, W., Meissner, K. J., Somes, C. J., Yao, W., & Oschlies, A. (2021). Explicit silicate cycling in the Kiel Marine Biogeochemistry Model version 3 (KMBM3) embedded in the UVic ESCM version 2.9. *Geoscientific Model Development*, *14*(12), 7255–7285. https://doi.org/10.5194/gmd-14-7255-2021

Lafond, A., Leblanc, K., Legras, J., Cornet, V., & Quéguiner, B. (2020). The structure of diatom communities constrains biogeochemical properties in surface waters of the Southern Ocean (Kerguelen Plateau). *Journal of Marine Systems*, *212*, 103458. https://doi.org/10.1016/j.jmarsys.2020.103458

Lambeck, K., Rouby, H., Purcell, A., Sun, Y., & Sambridge, M. (2014). Sea level and global ice volumes from the Last Glacial Maximum to the Holocene. *Proceedings of the National Academy of Sciences*, *111*(43), 15296–15303. https://doi.org/10.1073/pnas.1411762111

Lambert, F., Tagliabue, A., Shaffer, G., Lamy, F., Winckler, G., Farias, L., et al. (2015). Dust fluxes and iron fertilization in Holocene and Last Glacial Maximum climates. *Geophysical Research Letters*, *42*(14), 6014–6023. https://doi.org/10.1002/2015GL064250

Letscher, R. T., Hansell, D. A., Carlson, C. A., Lumpkin, R., & Knapp, A. N. (2013). Dissolved organic nitrogen in the global surface ocean: Distribution and fate. *Global Biogeochemical Cycles*, *27*(1), 141–153. https://doi.org/10.1029/2012GB004449

Liefer, J. D., Garg, A., Fyfe, M. H., Irwin, A. J., Benner, I., Brown, C. M., et al. (2019). The macromolecular basis of phytoplankton C:N:P under nitrogen starvation. *Frontiers in Microbiology*, *10*, 763. https://doi.org/10.3389/fmicb.2019.00763

Lønborg, C., Carreira, C., Jickells, T., & Álvarez-Salgado, X. A. (2020). Impacts of global change on ocean dissolved organic carbon (DOC) cycling. *Frontiers in Marine Science*, *7*, 466. https://doi.org/10.3389/fmars.2020.00466

Lüthi, D., Le Floch, M., Bereiter, B., Blunier, T., Barnola, J.-M., Siegenthaler, U., et al. (2008). High-resolution carbon dioxide concentration record 650,000–800,000 years before present. *Nature*, *453*(7193), 379–382. https://doi.org/10.1038/nature06949

1174 Marcott, S. A., Bauska, T. K., Buizert, C., Steig, E. J., Rosen, J. L., Cuffey, K. M., et al. (2014).
1175 Centennial-scale changes in the global carbon cycle during the last deglaciation. *Nature*,
1176 *514*(7524), 616–619. https://doi.org/10.1038/nature13799
1177 Martiny, A. C., Pham, C. T. A., Primeau, F. W., Vrugt, J. A., Moore, J. K., Levin, S. A., &
1178 Lomas, M. W. (2013). Strong latitudinal patterns in the elemental ratios of marine
1179 plankton and organic matter. *Nature Geoscience*, *6*(4), 279–283.
1180 https://doi.org/10.1038/ngeo1757
1181 Mather, R. L., Reynolds, S. E., Wolff, G. A., Williams, R. G., Torres-Valdes, S., Woodward, E.
1182 M. S., et al. (2008). Phosphorus cycling in the North and South Atlantic Ocean
1183 subtropical gyres. *Nature Geoscience*, *1*(7), 439–443. https://doi.org/10.1038/ngeo232
1184 Matsumoto, K. (2007). Biology-mediated temperature control on atmospheric pCO_2 and ocean
1185 biogeochemistry. *Geophysical Research Letters*, *34*(20), L20605.
1186 https://doi.org/10.1029/2007GL031301
1187 Matsumoto, K., Chase, Z., & Kohfeld, K. (2014). Different mechanisms of silicic acid leakage
1188 and their biogeochemical consequences. *Paleoceanography*, *29*(3), 238–254.
1189 https://doi.org/10.1002/2013PA002588
1190 Matsumoto, K., Rickaby, R., & Tanioka, T. (2020). Carbon export buffering and CO_2 drawdown
1191 by flexible phytoplankton C:N:P under glacial conditions. *Paleoceanography and*
1192 *Paleoclimatology*, *35*(7). https://doi.org/10.1029/2019PA003823
1193 Matsumoto, K., Tokos, K., Huston, A., & Joy-Warren, H. (2013). MESMO 2: a mechanistic
1194 marine silica cycle and coupling to a simple terrestrial scheme. *Geoscientific Model*
1195 *Development*, *6*(2), 477–494. https://doi.org/10.5194/gmd-6-477-2013
1196 McKinley, G. A., Fay, A. R., Lovenduski, N. S., & Pilcher, D. J. (2017). Natural variability and
1197 anthropogenic trends in the ocean carbon sink. *Annual Review of Marine Science*, *9*(1),
1198 125–150. https://doi.org/10.1146/annurev-marine-010816-060529
1199 Meissner, K. J., Weaver, A. J., Matthews, H. D., & Cox, P. M. (2003). The role of land surface
1200 dynamics in glacial inception: A study with the UVic Earth System Model. *Climate*
1201 *Dynamics*, *21*(7–8), 515–537. https://doi.org/10.1007/s00382-003-0352-2
1202 Mengis, N., Keller, D. P., MacDougall, A. H., Eby, M., Wright, N., Meissner, K. J., et al. (2020).
1203 Evaluation of the University of Victoria Earth System Climate Model version 2.10 (UVic
1204 ESCM 2.10). *Geoscientific Model Development*, *13*(9), 4183–4204.
1205 https://doi.org/10.5194/gmd-13-4183-2020
1206 Meyer, J., Löscher, C. R., Neulinger, S. C., Reichel, A. F., Loginova, A., Borchard, C., et al.
1207 (2016). Changing nutrient stoichiometry affects phytoplankton production, DOP
1208 accumulation and dinitrogen fixation – a mesocosm experiment in the eastern tropical
1209 North Atlantic. *Biogeosciences*, *13*(3), 781–794. https://doi.org/10.5194/bg-13-781-2016
1210 Meyerink, S. W., Ellwood, M. J., Maher, W. A., Dean Price, G., & Strzepek, R. F. (2017).
1211 Effects of iron limitation on silicon uptake kinetics and elemental stoichiometry in two
1212 Southern Ocean diatoms, *Eucampia antarctica* and *Proboscia inermis* , and the temperate
1213 diatom *Thalassiosira pseudonana*. *Limnology and Oceanography*, *62*(6), 2445–2462.
1214 https://doi.org/10.1002/lno.10578
1215 Microsoft Corporation. (2018). Microsoft Powerpoint. Retrieved from
1216 https://office.microsoft.com/powerpoint
1217 Mills, M. M., & Arrigo, K. R. (2010). Magnitude of oceanic nitrogen fixation influenced by the
1218 nutrient uptake ratio of phytoplankton. *Nature Geoscience*, *3*(6), 412–416.
1219 https://doi.org/10.1038/ngeo856

Monteiro, F. M., & Follows, M. J. (2012). On nitrogen fixation and preferential remineralization of phosphorus. *Geophysical Research Letters*, *39*(6), L06607. https://doi.org/10.1029/2012GL050897

Moore, C. M., Mills, M. M., Arrigo, K. R., Berman-Frank, I., Bopp, L., Boyd, P. W., et al. (2013). Processes and patterns of oceanic nutrient limitation. *Nature Geoscience*, *6*(9), 701–710. https://doi.org/10.1038/ngeo1765

Moore, J. K., Doney, S. C., & Lindsay, K. (2004). Upper ocean ecosystem dynamics and iron cycling in a global three-dimensional model. *Global Biogeochemical Cycles*, *18*(4), GB4028. https://doi.org/10.1029/2004GB002220

Moreno, A. R., Hagstrom, G. I., Primeau, F. W., Levin, S. A., & Martiny, A. C. (2018). Marine phytoplankton stoichiometry mediates nonlinear interactions between nutrient supply, temperature, and atmospheric CO_2; *Biogeosciences*, *15*(9), 2761–2779. https://doi.org/10.5194/bg-15-2761-2018

Moreno, A. R., & Martiny, A. C. (2018). Ecological stoichiometry of ocean plankton. *Annual Review of Marine Science*, *10*(1), 43–69. https://doi.org/10.1146/annurev-marine-121916-063126

Muglia, J., & Schmittner, A. (2015). Glacial atlantic overturning increased by wind stress in climate models. *Geophysical Research Letters*, *42*(22), 9862–9868. https://doi.org/10.1002/2015GL064583

Muglia, J., Skinner, L. C., & Schmittner, A. (2018). Weak overturning circulation and high Southern Ocean nutrient utilization maximized glacial ocean carbon. *Earth and Planetary Science Letters*, *496*, 47–56. https://doi.org/10.1016/j.epsl.2018.05.038

Muglia, J., Somes, C. J., Nickelsen, L., & Schmittner, A. (2017). Combined effects of atmospheric and seafloor iron fluxes to the glacial ocean. *Paleoceanography*, *32*(11), 1204–1218. https://doi.org/10.1002/2016PA003077

Nowicki, M., DeVries, T., & Siegel, D. A. (2022). Quantifying the carbon export and sequestration pathways of the ocean's biological carbon pump. *Global Biogeochemical Cycles*, *36*(3). https://doi.org/10.1029/2021GB007083

Ödalen, M., Nycander, J., Ridgwell, A., Oliver, K. I. C., Peterson, C. D., & Nilsson, J. (2020). Variable C/P composition of organic production and its effect on ocean carbon storage in glacial-like model simulations. *Biogeosciences*, *17*(8), 2219–2244. https://doi.org/10.5194/bg-17-2219-2020

Pahlow, M., Chien, C.-T., Arteaga, L. A., & Oschlies, A. (2020). Optimality-based non-Redfield plankton–ecosystem model (OPEM v1.1) in UVic-ESCM 2.9 – Part 1: Implementation and model behaviour. *Geoscientific Model Development*, *13*(10), 4663–4690. https://doi.org/10.5194/gmd-13-4663-2020

Peltier, W. R., Argus, D. F., & Drummond, R. (2015). Space geodesy constrains ice age terminal deglaciation: The global ICE-6G_C (VM5a) model. *Journal of Geophysical Research: Solid Earth*, *120*(1), 450–487. https://doi.org/10.1002/2014JB011176

Petit, J. R., Jouzel, J., Raynaud, D., Barkov, N. I., Delaygue, G., Delmotte, M., et al. (1999). Climate and atmospheric history of the past 420,000 years from the Vostok ice core, Antarctica. *Nature*, *399*, 429-436.

Prentice, I. C., Harrison, S. P., & Bartlein, P. J. (2011). Global vegetation and terrestrial carbon cycle changes after the last ice age. *New Phytologist*, *189*(4), 988–998. https://doi.org/10.1111/j.1469-8137.2010.03620.x

Ramaswamy, V., Chanin, M.-L., Angell, J., Barnett, J., Gaffen, D., Gelman, M., et al. (2001). Stratospheric temperature trends: Observations and model simulations. *Reviews of Geophysics*, *39*(1), 71–122. https://doi.org/10.1029/1999RG000065

Redfield, A.C. (1934) On the Proportions of Organic Derivatives in Sea Water and Their Relation to the Composition of Plankton. *James Johnstone Memorial Volume, University Press of Liverpool*, 176-192.

Redfield, A.C. (1958) The Biological Control of Chemical Factors in the Environment. *American Scientist*, 46, 205-221.

Sañudo-Wilhelmy, S. A., Tovar-Sanchez, A., Fu, F.X., Capone, D. G., Carpenter, E. J., & Hutchins, D. A. (2004). The impact of surface-adsorbed phosphorus on phytoplankton Redfield stoichiometry. *Nature*, *432*(7019), 897–901. https://doi.org/10.1038/nature03125

Sarmiento, J. L., & Gruber, N. (2006). *Ocean Biogeochemical Dynamics*. Princeton University Press.

Schmittner, A., Gruber, N., Mix, A. C., Key, R. M., Tagliabue, A., & Westberry, T. K. (2013). Biology and air–sea gas exchange controls on the distribution of carbon isotope ratios ($\delta^{13}C$) in the ocean. *Biogeosciences*, *10*(9), 5793–5816. https://doi.org/10.5194/bg-10-5793-2013

Schmittner, A., & Somes, C. J. (2016). Complementary constraints from carbon (^{13}C) and nitrogen (^{15}N) isotopes on the glacial ocean's soft-tissue biological pump. *Paleoceanography*, *31*(6), 669–693. https://doi.org/10.1002/2015PA002905

Séférian, R., Berthet, S., Yool, A., Palmiéri, J., Bopp, L., Tagliabue, A., et al. (2020). Tracking improvement in simulated marine biogeochemistry between CMIP5 and CMIP6. *Current Climate Change Reports*, *6*(3), 95–119. https://doi.org/10.1007/s40641-020-00160-0

Sigman, D. M., Hain, M. P., & Haug, G. H. (2010). The polar ocean and glacial cycles in atmospheric CO2 concentration. *Nature*, *466*(7302), 47–55. https://doi.org/10.1038/nature09149

Somes, C. J., & Oschlies, A. (2015). On the influence of "non-Redfield" dissolved organic nutrient dynamics on the spatial distribution of N_2 fixation and the size of the marine fixed nitrogen inventory. *Global Biogeochemical Cycles*, *29*(7), 973–993. https://doi.org/10.1002/2014GB005050

Somes, C. J., Schmittner, A., Galbraith, E. D., Lehmann, M. F., Altabet, M. A., Montoya, J. P., et al. (2010). Simulating the global distribution of nitrogen isotopes in the ocean. *Global Biogeochemical Cycles*, *24*(4), GB4019. https://doi.org/10.1029/2009GB003767

Somes, C. J., Schmittner, A., Muglia, J., & Oschlies, A. (2017). A Three-Dimensional Model of the Marine Nitrogen Cycle during the Last Glacial Maximum Constrained by Sedimentary Isotopes. *Frontiers in Marine Science*, 4. https://doi.org/10.3389/fmars.2017.00108

Tagliabue, A., Bopp, L., Roche, D. M., Bouttes, N., & Paillard, D. (2009). Quantifying the roles of ocean circulation and biogeochemistry in governing ocean carbon-13 and atmospheric carbon dioxide at the last glacial maximum. *Clim. Past*, *5,* 695 - 706, https://doi.org/10.5194/cp-5-695-2009

Takeda, S. (1998). Influence of iron availability on nutrient consumption ratio of diatoms in oceanic waters. *Nature*, *393*(6687), 774–777. https://doi.org/10.1038/31674

Tanioka, T., & Matsumoto, K. (2017). Buffering of ocean export production by flexible elemental stoichiometry of particulate organic matter. *Global Biogeochemical Cycles*, *31*(10), 1528–1542. https://doi.org/10.1002/2017GB005670

Tanioka, T., & Matsumoto, K. (2020). A meta-analysis on environmental drivers of marine phytoplankton C:N:P. *Biogeosciences*, *17*(11), 2939–2954. https://doi.org/10.5194/bg-17-2939-2020

Taylor, K.E. (2001). Summarizing multiple aspects of model performance in a single diagram. *Journal of Geophysical Research. D. Atmospheres*, *106*(D7), 7183–7192. https://doi.org/10.1029/2000JD900719

Tesdal, Galbraith, E. D., & Kienast, M. (2013). Nitrogen isotopes in bulk marine sediment: linking seafloor observations with subseafloor records. *Biogeosciences*, *10*(1), 101–118. https://doi.org/10.5194/bg-10-101-2013

Tierney, J. E., Poulsen, C. J., Montañez, I. P., Bhattacharya, T., Feng, R., Ford, H. L., et al. (2020). Past climates inform our future. *Science*, *370*(6517), aay3701. https://doi.org/10.1126/science.aay3701

Toggweiler, J. R. (1999). Variation of atmospheric CO_2 by ventilation of the ocean's deepest water. *Paleoceanography*, *14*(5), 571–588. https://doi.org/10.1029/1999PA900033

Tyrrell, T. (1999). The relative influences of nitrogen and phosphorus on oceanic primary production. *Nature*, *400*, 525-531.

Volk, T., & Hoffert, M. I. (1985). Ocean carbon pumps: analysis of relative strengths and efficiencies in ocean-driven atmospheric CO_2 changes. In E. T. Sundquist & W. S. Broecker (Eds.), *Geophysical Monograph Series* (pp. 99–110). American Geophysical Union. https://doi.org/10.1029/GM032p0099

Wagner, S., Schubotz, F., Kaiser, K., Hallmann, C., Waska, H., Rossel., et al. (2020). Soothsaying DOM: A current perspective on the future of oceanic dissolved organic carbon. *Frontiers in Marine Science*, *7*, 341. https://doi.org/10.3389/fmars.2020.00341

Ward, B. A., Dutkiewicz, S., Moore, C. M., & Follows, M. J. (2013). Iron, phosphorus, and nitrogen supply ratios define the biogeography of nitrogen fixation. *Limnology and Oceanography*, *58*(6), 2059–2075. https://doi.org/10.4319/lo.2013.58.6.2059

Weaver, A. J., Eby, M., Wiebe, E. C., Bitz, C. M., Duffy, P. B., Ewen, T. L., et al. (2001). The UVic earth system climate model: Model description, climatology, and applications to past, present and future climates. *Atmosphere-Ocean*, *39*(4), 361–428. https://doi.org/10.1080/07055900.2001.9649686

Weber, T. S., & Deutsch, C. (2010). Ocean nutrient ratios governed by plankton biogeography. *Nature*, *467*(7315), 550–554. https://doi.org/10.1038/nature09403

White, A. E., Spitz, Y. H., Karl, D. M., & Letelier, R. M. (2006). Flexible elemental stoichiometry in *Trichodesmium* spp. and its ecological implications. *Limnology and Oceanography*, *51*(4), 1777–1790. https://doi.org/10.4319/lo.2006.51.4.1777

Williams, P. M., & Druffel, E. R. M. (1987). Radiocarbon in dissolved organic matter in the central North Pacific Ocean. *Nature*, *330*(6145), 246–248. https://doi.org/10.1038/330246a0

Wu, J., Sunda, W., Boyle, E. A., & Karl, D. M. (2000). Phosphate depletion in the western North Atlantic Ocean. *Science*, *289*(5480), 759–762. https://doi.org/10.1126/science.289.5480.759

Yvon-Durocher, G., Jones, J. I., Trimmer, M., Woodward, G., & Montoya, J. M. (2010). Warming alters the metabolic balance of ecosystems. *Phil. Trans. R. Soc. B*, *365*(1549), 2117–2126. https://doi.org/10.1098/rstb.2010.0038

Zeng, N. (2003). Glacial-interglacial atmospheric CO2 change—The glacial burial hypothesis. *Advances in Atmospheric Sciences*, *20*(5), 677–693. https://doi.org/10.1007/BF02915395

Zúñiga, D., Sanchez-Vidal, A., Flexas, M. M., Carroll, D., Rufino, M. M., Spreen, G., et al. (2021). Sinking diatom assemblages as a key driver for deep carbon and silicon export in the Scotia Sea (Southern Ocean). *Front. Earth Sci.*, *9*, 579198. https://doi.org/10.3389/feart.2021.579198

References from the Supporting Information

Buchanan, P. J., Matear, R. J., Chase, Z., Phipps, S. J., & Bindoff, N. L. (2019). Ocean carbon and nitrogen isotopes in CSIRO Mk3L-COAL version 1.0: A tool for palaeoceanographic research. *Geoscientific Model Development*, *12*(4), 1491–1523. https://doi.org/10.5194/gmd-12-1491-2019

Galbraith, E. D., Gnanadesikan, A., Dunne, J. P., & Hiscock, M. R. (2010). Regional impacts of iron-light colimitation in a global biogeochemical model. *Biogeosciences*, 7(3), 1043-1064. https://doi.org/10.5194/bg-7-1043-2010

Galbraith, E. D., Kienast, M., & The NICOPP working group members. (2013). The acceleration of oceanic denitrification during deglacial warming. *Nature Geoscience*, *6*(7), 579–584. https://doi.org/10.1038/ngeo1832

Galbraith, E. D., & Martiny, A. C. (2015). A simple nutrient-dependence mechanism for predicting the stoichiometry of marine ecosystems. *Proceedings of the National Academy of Sciences*, *112*(27), 8199–8204. https://doi.org/10.1073/pnas.1423917112

Garcia, H. E., Locarnini, R. A., Boyer, T. P., Antonov, J. I., Baranova, O. K., Zweng, M. M., et al. (2013). World ocean atlas 2013. Volume 4, Dissolved inorganic nutrients (phosphate, nitrate, silicate). *NOAA Atlas NESDIS 76* https://doi.org/10.7289/V5J67DWD

Gruber, N., & Sarmiento, J. L. (1997). Global patterns of marine nitrogen fixation and denitrification. *Global Biogeochemical Cycles*, *11*(2), 235–266. https://doi.org/10.1029/97GB00077

Lambeck, K., Rouby, H., Purcell, A., Sun, Y., & Sambridge, M. (2014). Sea level and global ice volumes from the Last Glacial Maximum to the Holocene. *Proceedings of the National Academy of Sciences*, *111*(43), 15296–15303. https://doi.org/10.1073/pnas.1411762111

Letscher, R. T., Hansell, D. A., Carlson, C. A., Lumpkin, R., & Knapp, A. N. (2013). Dissolved organic nitrogen in the global surface ocean: Distribution and fate. *Global Biogeochemical Cycles*, *27*(1), 141–153. https://doi.org/10.1029/2012GB004449

Mather, R. L., Reynolds, S. E., Wolff, G. A., Williams, R. G., Torres-Valdes, S., Woodward, E. M. S., et al. (2008). Phosphorus cycling in the North and South Atlantic Ocean subtropical gyres. *Nature Geoscience*, *1*(7), 439–443. https://doi.org/10.1038/ngeo232

Muglia, J., Skinner, L. C., & Schmittner, A. (2018). Weak overturning circulation and high Southern Ocean nutrient utilization maximized glacial ocean carbon. *Earth and Planetary Science Letters*, *496*, 47–56. https://doi.org/10.1016/j.epsl.2018.05.038

Muglia, J., Somes, C. J., Nickelsen, L., & Schmittner, A. (2017). Combined Effects of Atmospheric and Seafloor Iron Fluxes to the Glacial Ocean. *Paleoceanography*, *32*(11), 1204–1218. https://doi.org/10.1002/2016PA003077

1397 Sarmiento, J. L., & Gruber, N. (2006). *Ocean biogeochemical dynamics*. Princeton University
1398 Press.
1399 Schmittner, A., & Somes, C. J. (2016). Complementary constraints from carbon (^{13}C) and
1400 nitrogen (^{15}N) isotopes on the glacial ocean's soft-tissue biological pump.
1401 *Paleoceanography*, *31*(6), 669–693. https://doi.org/10.1002/2015PA002905
1402 Somes, C. J., & Oschlies, A. (2015). On the influence of "non-Redfield" dissolved organic
1403 nutrient dynamics on the spatial distribution of N_2 fixation and the size of the marine
1404 fixed nitrogen inventory. *Global Biogeochemical Cycles*, *29*(7), 973–993.
1405 https://doi.org/10.1002/2014GB005050
1406 Somes, C. J., Schmittner, A., Galbraith, E. D., Lehmann, M. F., Altabet, M. A., Montoya, J. P., et
1407 al. (2010). Simulating the global distribution of nitrogen isotopes in the ocean. *Global*
1408 *Biogeochemical Cycles*, *24*(4). https://doi.org/10.1029/2009GB003767
1409 Tagliabue, A., Bopp, L., Roche, D. M., Bouttes, N., & Paillard, D. (2009). Quantifying the roles
1410 of ocean circulation and biogeochemistry in governing ocean carbon-13 and atmospheric
1411 carbon dioxide at the last glacial maximum. *Clim. Past*, *5,* 695 - 706,
1412 https://doi.org/10.5194/cp-5-695-2009
1413 Tesdal, Galbraith, E. D., & Kienast, M. (2013). Nitrogen isotopes in bulk marine sediment:
1414 linking seafloor observations with subseafloor records. *Biogeosciences*, *10*(1), 101–118.
1415 https://doi.org/10.5194/bg-10-101-2013